



## **Invigoration and Capping of a Convective Rainband ahead of a Potential Vorticity Anomaly**

GERAINT VAUGHAN

*National Centre for Atmospheric Science, and School of Earth and Environmental Sciences, University of Manchester, Manchester, United Kingdom*

BOGDAN ANTONESCU, DAVID M. SCHULTZ, AND CHRISTOPHER DEARDEN

*School of Earth and Environmental Sciences, University of Manchester, Manchester, United Kingdom*

(Manuscript received 17 October 2016, in final form 30 January 2017)


### ABSTRACT

Deep convection frequently occurs on the eastern side of upper-level troughs, or potential vorticity (PV) anomalies. This is consistent with uplift ahead of a cyclonic PV anomaly, and consequent reduction in static stability and increase of convective available potential energy (CAPE). Nevertheless, the causal link between upper-level PV and deep convection has not been proven, and given that lift, moisture, and instability must all be present for deep convection to occur it is not clear that upper-level forcing is sufficient. In this paper a convective rainband that intensified ahead of a cyclonic PV anomaly in an environment with little CAPE ( $\sim 10 \text{ J kg}^{-1}$ ) is examined to determine the factors responsible for its intensification. The key feature was a low-level convergence line, arising from the remnants of an occluded front embedded in the low-level cyclonic flow. The rainband's intensity and morphology was influenced by the remnants of a tropopause fold that capped convection at midlevels in the southern part of the band, and by a reduction in upper-level static stability in the northern part of the band that allowed the convection to reach the tropopause. Ascent ahead of the trough appears to have played only a minor role in conditioning the atmosphere to convection: in most cases the ascending airstream had previously descended in the flow west of the trough axis. Thus, simple "PV thinking" is not capable of describing the development of the rainband, and it is concluded that preexisting low-level wind and humidity features played the dominant role.

### 1. Introduction

Downstream of an upper-level trough in the extratropics, there is synoptic-scale ascent in an environment of reduced static stability, favoring both frontal development and deep convection. Viewed from a potential vorticity (PV) perspective, the ascent is a response to a cyclonic upper-level PV anomaly, a region of locally depressed stratospheric air. Isentropic surfaces in the troposphere bow upward toward the anomaly, causing

air to ascend ahead of it and subside behind it as the anomaly moves (Hoskins et al. 1985). The mechanism was further clarified by Hoskins et al. (2003) who introduced the concepts of *isentropic upglide* (the vacuum-cleaner effect) for the motion of air on tilted isentropic surfaces and *isentropic displacement* for the development of an anomaly over time. In this picture, a cyclonic PV anomaly at tropopause level moving from west to east will be associated with ascending motion, and

 Denotes content that is immediately available upon publication as open access.

*Publisher's Note:* This article was revised on 6 September 2017 to include the CC BY license that was missing when originally published.

*Corresponding author e-mail:* Prof. Geraint Vaughan, geraint.vaughan@manchester.ac.uk



This article is licensed under a [Creative Commons Attribution 4.0 license](http://creativecommons.org/licenses/by/4.0/) (<http://creativecommons.org/licenses/by/4.0/>).

DOI: 10.1175/MWR-D-16-0397.1

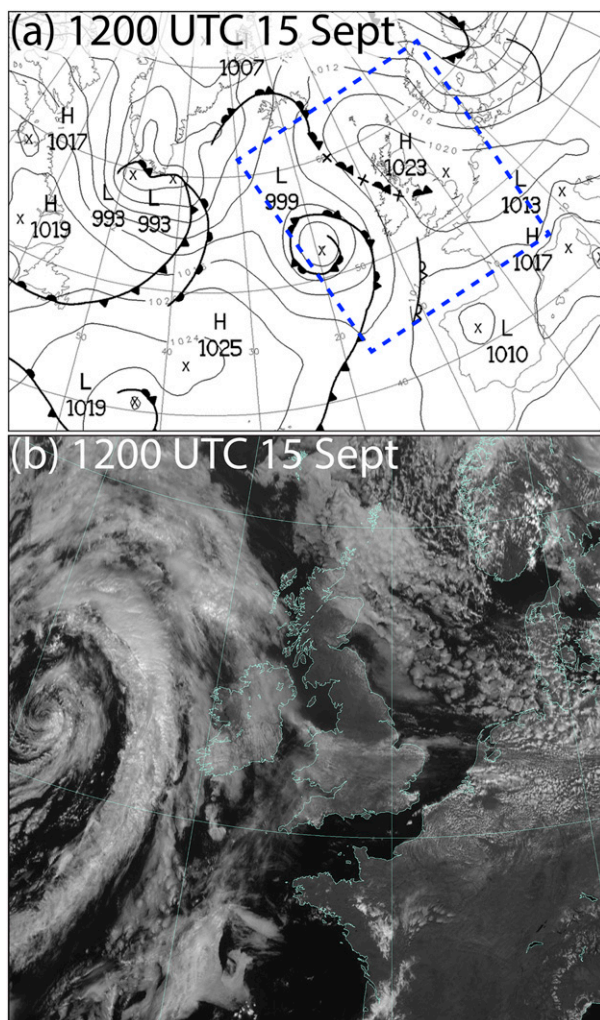


FIG. 1. (a) Sea level pressure chart for 1200 UTC 15 Sep 2011. The blue dashed box represents the location of (b). (b) Corresponding visible satellite image from Meteosat Second Generation (MSG). The crosses on the occluded front in (a) denote a dissipating feature; open symbols denote a front above the surface.

hence a tendency for clouds and precipitation, on its leading flank. Further, these effects in principle extend throughout the troposphere, decreasing the atmospheric stability and potentially increasing the convective available potential energy (CAPE), thus creating an environment more favorable for deep convection (Jukes and Smith 2000; Nielsen-Gammon and Gold 2008). A cyclonic PV anomaly also induces cyclonic flow beneath it (Hoskins et al. 1985), leading to low-level flow that can advect warm, moist air into the region ahead of the trough.

Indeed, in the subtropics, there is considerable evidence for extensive convection on the eastern side of midlatitude troughs that move toward the tropics (Waugh and Polvani 2000; Waugh and Funatsu 2003; Waugh 2005;

Funatsu and Waugh 2008; Sandhya and Sridharan 2014). Deep convection in the midlatitudes can also be associated with cyclonic upper-level PV anomalies. For example, Antonescu et al. (2013) examined the distribution of convection around upper-level troughs passing over the United Kingdom, using a wind-profiling radar to identify tropopause folds and the Met Office's weather radar network to identify convective storms. Convection was twice as prevalent on the eastern side of a trough as on the western side, and also tended to be organized into multicellular lines ahead of the trough. This result is consistent with that reported by Schumann and Roebber (2010) who found that multicellular convection in the central United States tended to occur in environments with strong, elongated upper-level PV anomalies.

How does this conceptual model for PV thinking overlap with that for deep moist convection? Specifically, all environments favorable for deep moist convection are characterized by three necessary and sufficient ingredients: moisture, low static stability, and a lifting mechanism for the parcels to ascend to their level of free convection (LFC) (Johns and Doswell 1992; Doswell and Bosart 2001). Although the cyclonic upper-level PV anomaly is associated with reduced static stability throughout the troposphere (and hence the likelihood of increased CAPE; Nielsen-Gammon and Gold 2008), the lifting provided by synoptic-scale processes like isentropic upglide is insufficient to initiate convection on realistic time scales of a few hours (Doswell and Bosart 2001). Gold and Nielsen-Gammon (2008), examining a tornado outbreak near Oklahoma City, Oklahoma, concluded from experiments with PV inversion that increasing the upper-level PV anomaly enhances CAPE downstream of it, but has little effect on winds near the lower boundary. Further, Schlemmer et al. (2010), examining a PV streamer approaching the Alps (a recognized harbinger of heavy convective rainfall), concluded that, although the streamer decreased the static stability throughout the troposphere directly beneath it, "destabilization [was] a second-order effect in the formation of heavy precipitation in the Alps" (p. 2352). Understanding the low-level conditions (moisture and stability) and low-level lifting mechanisms is therefore a prerequisite to understanding how convection develops downstream of an upper-level trough. The primary question addressed in this paper is whether these factors are sufficient in themselves to explain the observed convective organization, or whether the upper-level PV anomaly also played a part: does the convection self-organize under synoptic forcing or does the observed organization develop in response to some preexisting susceptibility on a smaller scale?

A further aspect of cyclonic upper-level PV anomalies that may enhance or limit the development of

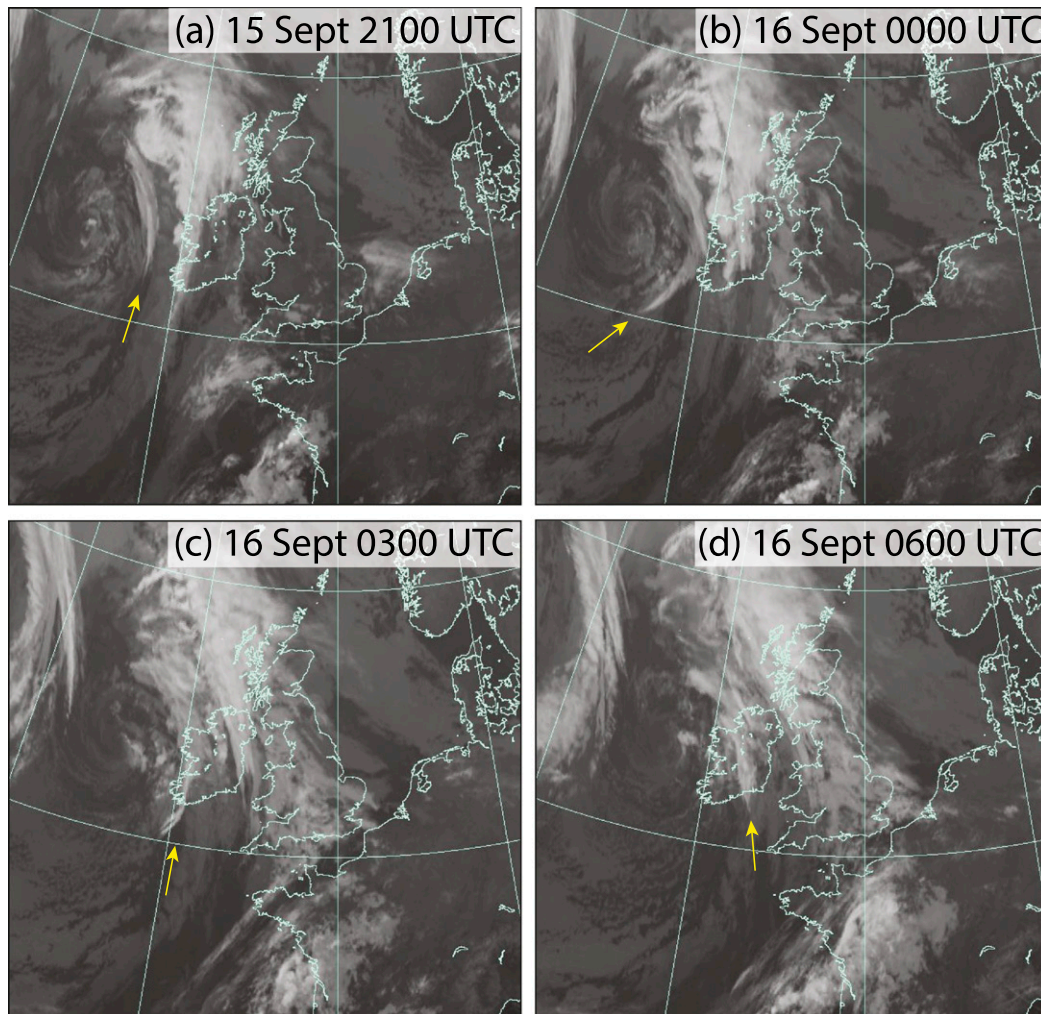


FIG. 2. MSG infrared images at (a) 2100 UTC 15 Sep, (b) 0000 UTC 16 Sep, (c) 0300 UTC 16 Sep, and (d) 0600 UTC 16 Sep. Arrows point to the convective band discussed in this paper.

convective storms is their associated tropopause folds. Often formed and most prominent on the western side of a trough (Reed and Sanders 1953; Newton 1954; Reed 1955; Newton 1958), the fold also extends around to the eastern side creating conditions of potential instability as the very dry stratospheric air in the fold flows over moist boundary layer air (Danielsen 1968). Because of the synoptic-scale ascent downstream of the trough, the convective inhibition of the fold is reduced and potential instability can be released if sufficient local lifting is present in the boundary layer (Browning and Roberts 1994; Browning et al. 1996). However, the fold can also cap or suppress convection (Reid and Vaughan 2004; Russell et al. 2012). In addition, remnants of folds from previous systems can become entangled in a cyclone and either cap convection (Russell et al. 2008) or promote convection at one level and cap

at another (Russell et al. 2009), making the prediction of convection in individual cases dependent on the detailed properties of layers of convective inhibition (Browning et al. 2007).

This article explores the development of an organized band of showers that formed downstream of an upper-level trough over Ireland and Wales on 16 September 2011. We examine the cause of the organization and the part played by isentropic upglide and isentropic displacement in creating the environment where convection occurred. Given that synoptic-scale ascent (such as isentropic upglide) is considered insufficient to initiate convection (Doswell and Bosart 2001), we examine whether the low-level convergence field may be responsible for both initializing and organizing the convective rainband. In doing so, we show that the cyclonic upper-level PV anomaly was



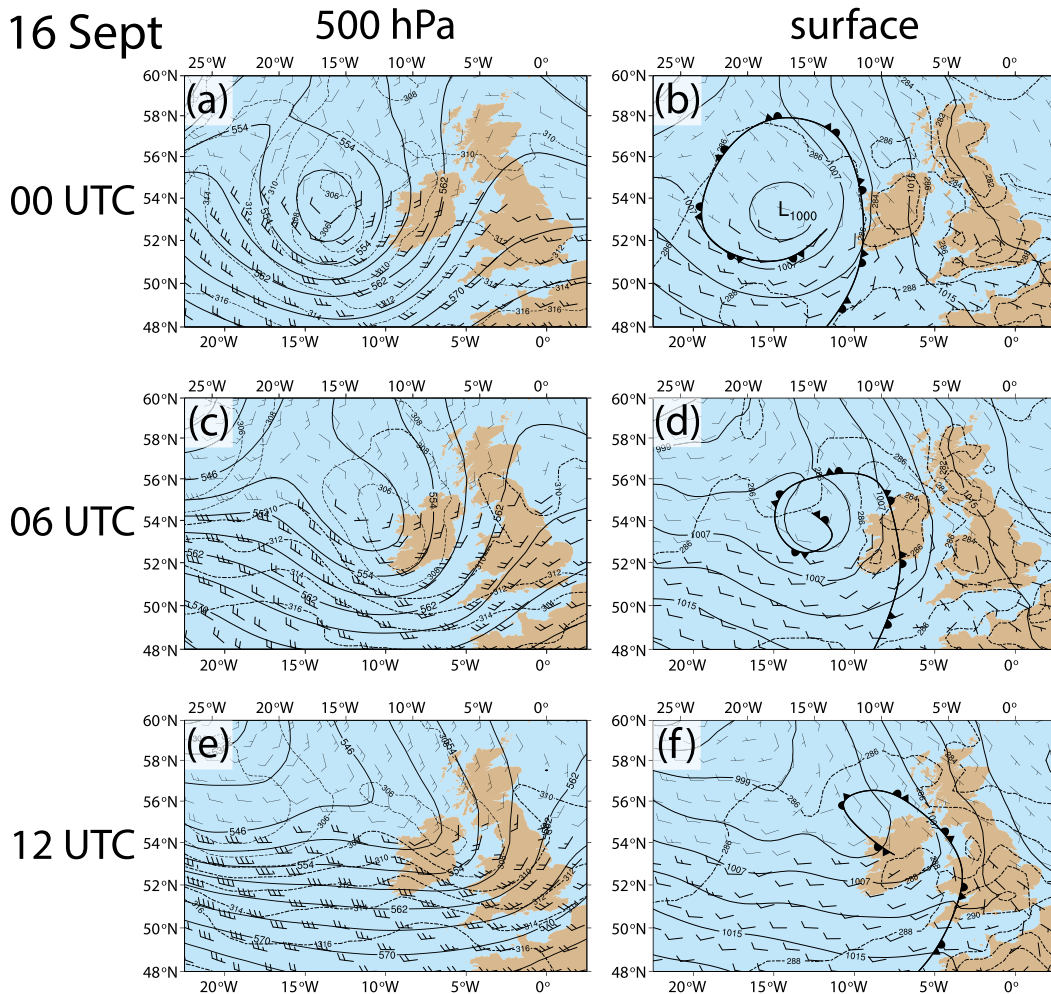


FIG. 3. Global Forecast System (GFS) analyses for 16 Sep 2011. 500-hPa geopotential height (solid lines every 4 dam), 500-hPa potential temperature (dashed lines every 1 K), and 500-hPa wind (one pennant, full barb, and half-barb denote 25, 5, and  $2.5 \text{ m s}^{-1}$ , respectively) at (a) 0000, (c) 0600, and (e) 1200 UTC. Sea level pressure (solid lines every 4 hPa), surface potential temperature (dashed lines every 2 K), 10-m wind (as for 500-hPa wind), and conventional frontal analysis from the Met Office at (b) 0000, (d) 0600, and (f) 1200 UTC.

responsible for lowering the upper-tropospheric static stability, enabling the convection to rise to the tropopause. Also, we show how convection in the southern part of the rainband was capped by the remnants of an upstream tropopause fold, adding to the evidence of Russell et al. (2008, 2009) that thin stable layers of stratospheric origin are important agents of convective inhibition in synoptic weather systems. These results serve to challenge the perception that convection develops downstream of an upper-level trough as a direct response to forcing by the PV anomaly.

The case study was chosen because it occurred during the first intensive observation period (IOP 1) of the Tropopause Folding, Stratospheric Intrusions and Deep Convection (TROSIAD) and the Diabatic

Influence on Mesoscale Structures in Extratropical Storms (DIAMET; Vaughan et al. 2015) projects when extra observations were available from aircraft and ground-based stations. Although a band of showers was forecast by the Met Office up to two days ahead, neither the location nor the tight organization of the convection was well captured, with the high-resolution version of the Unified Model tending to produce much more widespread convection than actually happened. Even the short-range (up to 12 h) convection-permitting forecasts initiated on 16 September predicted a broad area of convection ahead of the upper-level PV anomaly rather than the narrow rainband that was observed (not shown). As the present study will show, evolution of the rainband was dominated by the low-level wind field, so



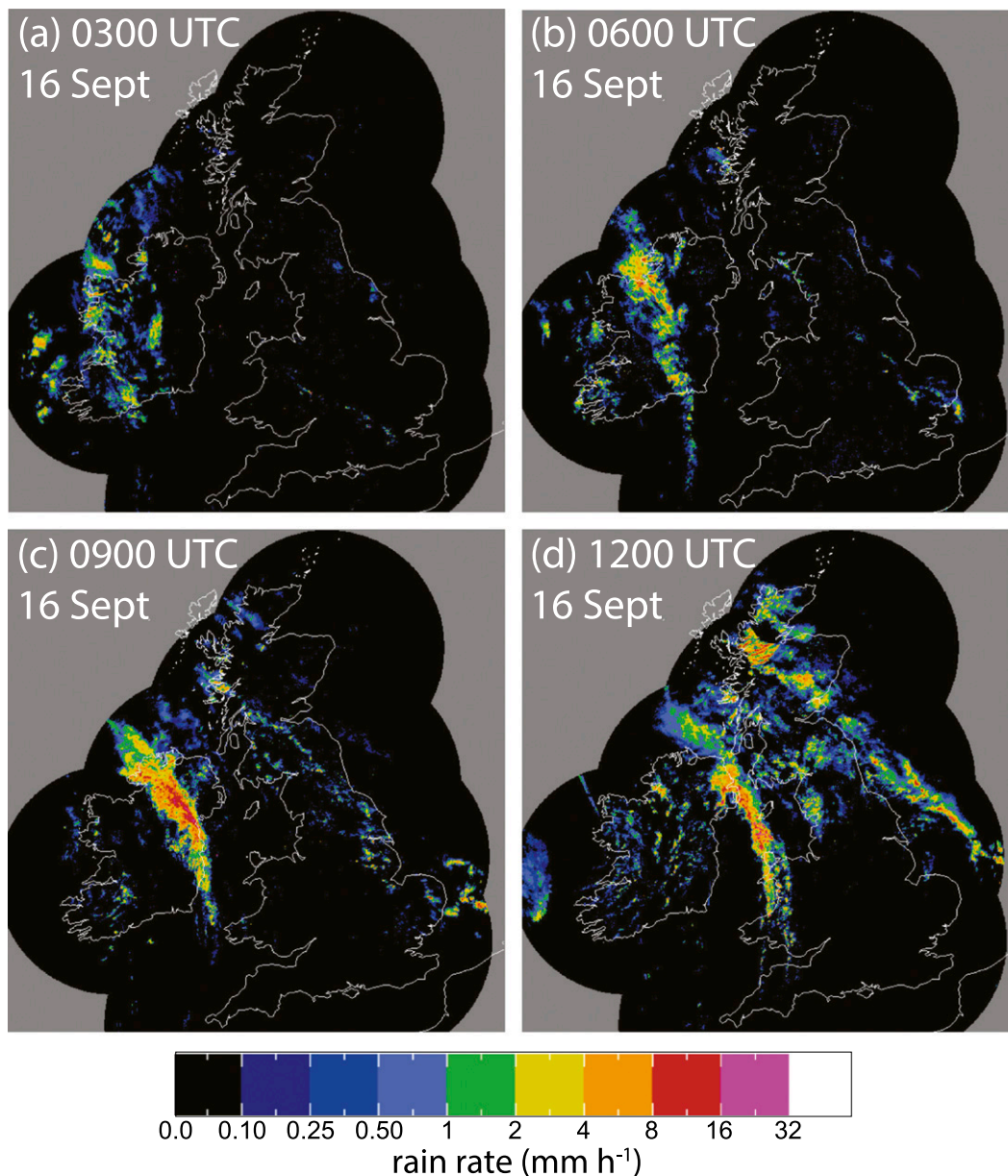


FIG. 4. Rain rate ( $\text{mm h}^{-1}$ , shaded according to the scale) from the U.K. weather radar network at (a) 0300, (b) 0600, (c) 0900, and (d) 1200 UTC 16 Sep.

that accurate representation of small-scale features in a data-sparse area was necessary for accurate forecasting of the rainband.

Section 2 describes the datasets and mesoscale model simulation used in this study. Operational and campaign observations used in this study are described in sections 2a and 2b, respectively. The model and its configuration for this study are described in section 2c. An overview of the synoptic and mesoscale environment in which the rainband evolved is provided in section 3, and the aircraft observations for this event are

discussed in section 4. Analysis of the model simulation is presented in section 5. Finally, the results of this paper are summarized in section 6.

## 2. Observations and model

### a. Operational observations

To identify the location of the rainband in this case, we use the Met Office’s weather radar network (Golding 1998; Harrison et al. 2009), which provides

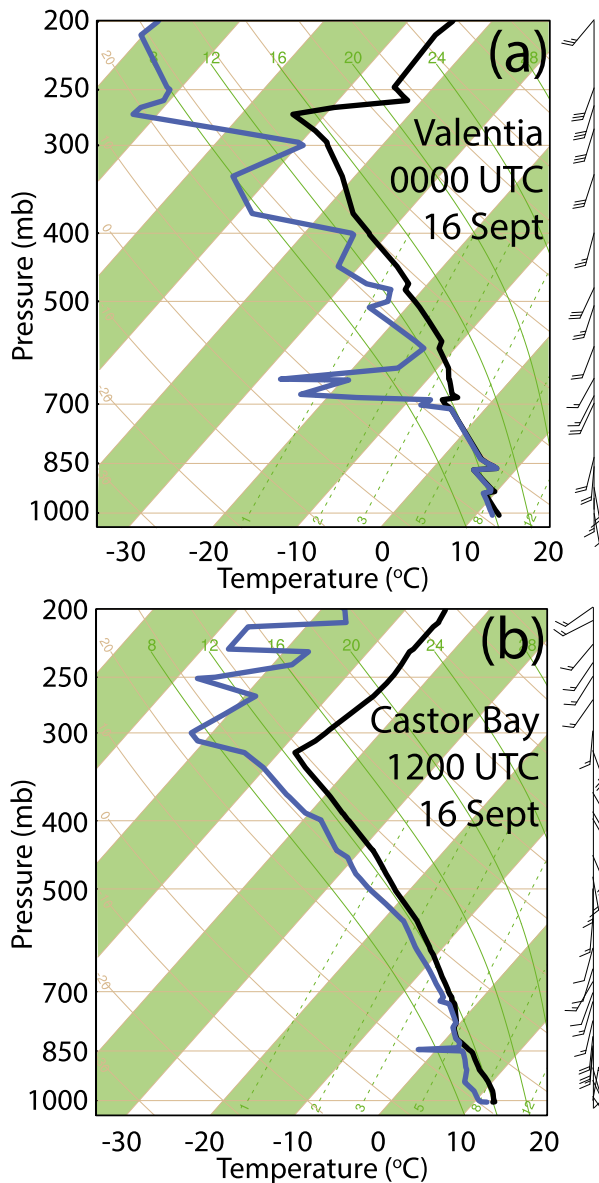


FIG. 5. Skew  $T$ -log $p$  plots of temperature (black solid lines) and dewpoint temperature (blue solid lines) for 16 Sep 2011: (a) Valentia at 0000 UTC and (b) Castor Bay at 1200 UTC. Horizontal wind is represented using pennant, barb, and half-barb denoting wind speeds of 25, 5, and  $2.5 \text{ m s}^{-1}$ , respectively. Locations of the two stations are shown in Fig. 9.

composite rain rate at 15-min intervals over the United Kingdom and Ireland with 1-km grid spacing (Kitchen and Illingworth 2011). The vertical structure of the atmosphere was monitored using the U.K. Mesosphere–Stratosphere–Troposphere (MST) radar (Vaughan 2002), a VHF wind-profiling radar operating at a frequency of 46.5 MHz and located at Capel Dewi ( $52.42^\circ\text{N}$ ,  $4.01^\circ\text{W}$ ) near Aberystwyth in mid-Wales (see Fig. 9 for the location of Capel Dewi). MST radar data

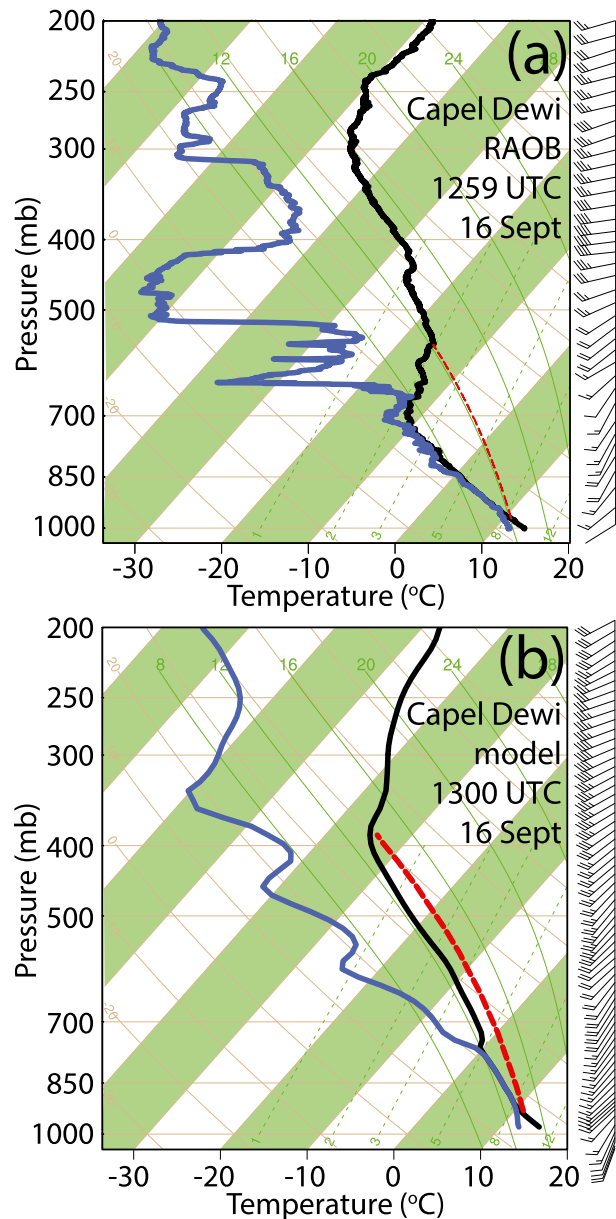


FIG. 6. Skew  $T$ -log $p$  plots of temperature (black solid lines) and dewpoint temperature (blue solid lines) for 16 Sep 2011 from Capel Dewi based on (a) radiosonde data at 1259 UTC and (b) WRF simulation at 1300 UTC. Horizontal wind is represented using pennant, barb, and half-barb denoting wind speeds of 25, 5, and  $2.5 \text{ m s}^{-1}$ , respectively. The area between the black solid line and the red dashed line represents CAPE. Location of Capel Dewi is shown in Fig. 9.

can be used to identify tropopause folds based on measurements of echo power [due to quasi-specular reflection from gradients in static stability and specific humidity; Gage and Green (1978)], wind shear, and wind speed (e.g., Rao et al. 2008; Antonescu et al. 2013).

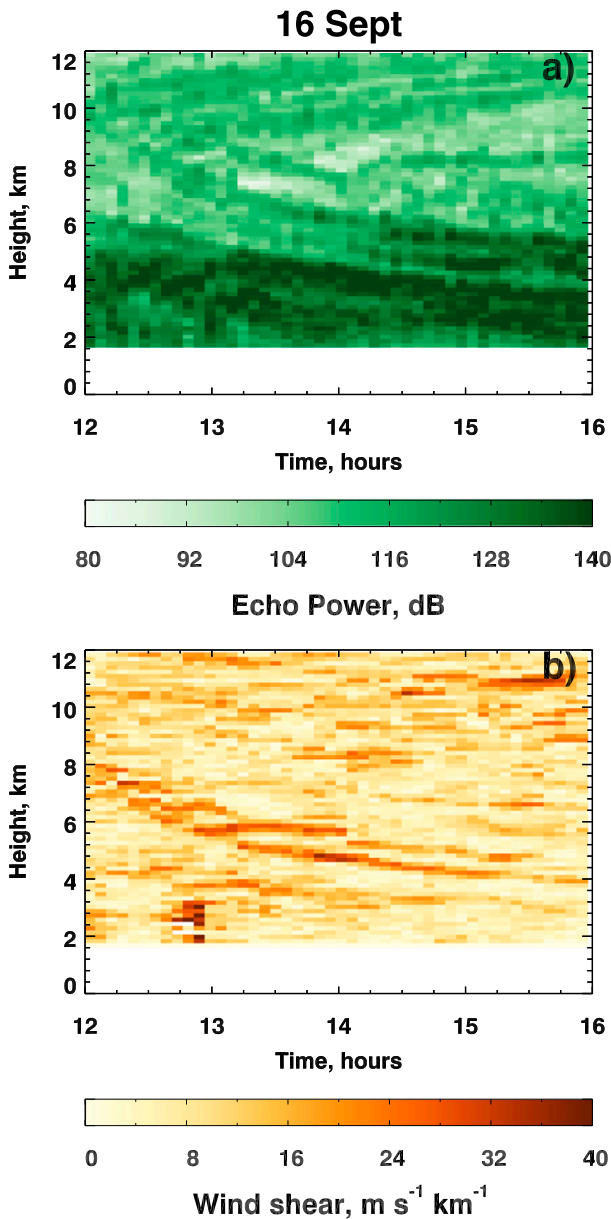


FIG. 7. Time–height cross sections of (a) echo power (dB, shaded according to the scale) and (b) vertical wind shear ( $\text{m s}^{-1} \text{km}^{-1}$ , shaded according to the scale) measured by the MST radar on 16 Sep 2011. The figures show the passage of the convective rainband (increase in power and wind shear up to 3 km just before 1300 UTC), the capping inversion around 4 km (layer of enhanced wind shear), and the tropopause fold on the western side of the PV anomaly (enhanced shear layer extending down from 8 km at 1200 UTC).

### b. Campaign observations

On 16 September 2011, during TROSIAD and DIAMET IOP 1, the Facility for Airborne Atmospheric Measurements (FAAM) BAe-146 research aircraft was used to measure in situ meteorological data,

microphysics, and chemical species over Ireland and the Irish Sea [the aircraft and instruments are described in Vaughan et al. (2015)]. Detailed observations of the rainband were also available from intensive ground-based observations at Capel Dewi, where radiosondes were launched at 0717, 1014, 1300, 1637, and 1902 UTC, supplementing the regular observations from Valentia in southwest Ireland ( $51.93^{\circ}\text{N}$ ,  $10.25^{\circ}\text{W}$ ) and Castor Bay in northeast Ireland ( $54.50^{\circ}\text{N}$ ,  $6.34^{\circ}\text{W}$ ) at 0000, 0600, and 1200 UTC (see Fig. 9 for the location of Valentia and Castor Bay).

### c. Model simulation

The rainband on 16 September 2011 was simulated using the Advanced Research version of the Weather Research and Forecasting Model (hereafter WRF; Skamarock et al. 2008) version 3.3.1, a compressible, nonhydrostatic, three-dimensional mesoscale model. The simulation used a single  $356 \times 266$  gridpoint domain with 9-km horizontal grid spacing and 100 vertical levels. Initial and lateral boundary conditions came from the  $0.25^{\circ}$  European Centre for Medium-Range Weather Forecasts (ECMWF) analyses. The simulation was initialized at 0000 UTC 15 September 2011 and run for 42 h with output every 30 min. The two-moment Morrison bulk microphysics scheme (Morrison et al. 2005, 2009) was used together with the Kain–Fritsch cumulus parameterization (Kain and Fritsch 1990, 1993; Kain 2004) to represent subgrid-scale convective precipitation. Other parameterizations included the Yonsei University planetary boundary layer scheme (Hong et al. 2006), the unified Noah land surface model (Chen and Dudhia 2001; Ek et al. 2003), and the shortwave (Dudhia 1989) and Rapid Radiative Transfer Model (RRTM) longwave radiation (Mlawer et al. 1997) schemes.

## 3. Synoptic and mesoscale overview

At 1200 UTC 15 September, the sea level pressure chart showed a low pressure center (999 hPa) at  $52^{\circ}\text{N}$ ,  $19^{\circ}\text{W}$ , around which was wrapped an occluded front manifest as a band of cloud on the visible satellite image (Fig. 1). To the east, over the United Kingdom, high pressure prevailed, with the center of the anticyclone around  $53^{\circ}\text{N}$ ,  $1^{\circ}\text{E}$ . Over the subsequent 12 h, the low pressure moved slowly eastward, with the center reaching  $53^{\circ}\text{N}$ ,  $15^{\circ}\text{W}$  by 0000 UTC 16 September. The progress of the cloud band is shown by infrared satellite images in Fig. 2. At 2100 UTC 15 September a band of low- to medium-level cloud extended along  $10^{\circ}\text{W}$ , with its leading edge over the west of Ireland (Fig. 2a). A prominent band of high cloud lay on its eastern flank, increasing in extent toward the north. This band



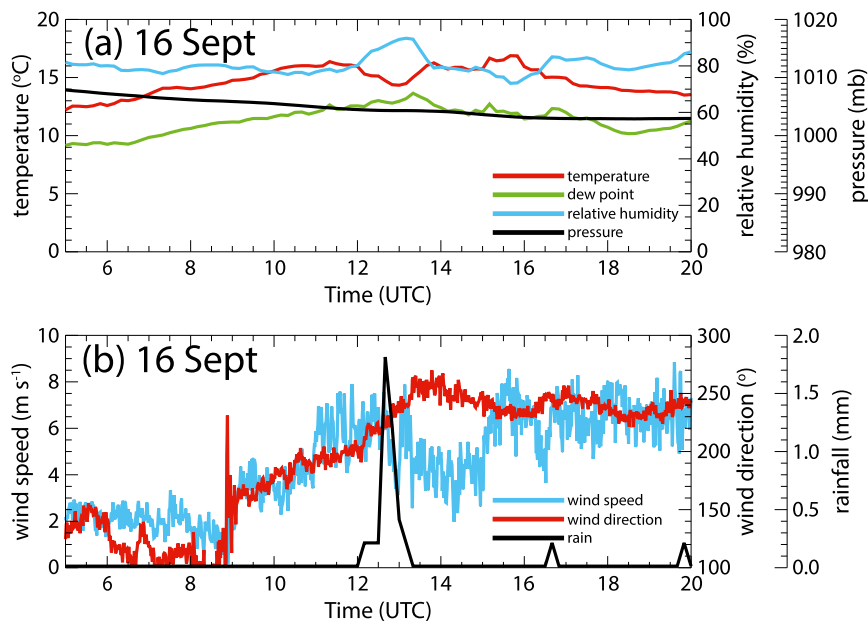


FIG. 8. Surface measurements at Capel Dewi on 16 Sep 2011: (a) temperature (°C, red line), dewpoint temperature (°C, green line), relative humidity (%), and pressure (hPa, black line), and (b) wind speed ( $\text{m s}^{-1}$ , blue line), wind direction (°, red line), and rainfall accumulation every 10 min (mm, black line).

developed what appears to be a horizontal shear instability between 2100 UTC 15 September and 0000 UTC 16 September (Figs. 2a and 2b, around 10°W), and dissipated within a few hours. Of more relevance to this study was a smaller band of high cloud that remained at the western edge of the lower-level cloud (e.g., along 10°W in Fig. 2c), and thickened over time. This band lay across Ireland by 0600 UTC 16 September (Fig. 2d).

Associated with the surface low pressure system was an upper-level trough with a closed circulation at 500 hPa and a prominent ridge ahead of it over the United Kingdom (Fig. 3a). From 0000 to 1200 UTC 16 September, the trough moved eastward, lost its closed circulation, and developed a pronounced northwest-southeast tilt (Figs. 3c,e). This cyclonic rotation of the trough axis occurred as the trough weakened as it approached the strengthening downstream ridge (Figs. 3a,c,e). The surface flow broadly matched that at 500 hPa, with the closed cyclone at 0000 UTC moving eastward and weakening over the subsequent 12 h, ending with a broad trough tilted northwest-southeast over the British Isles (Figs. 3b,d,f).

The rainband that is the focus of this paper first appeared in the radar imagery as an area of unorganized convective cells over western Ireland (Fig. 4a), coinciding with the low-medium cloud band on the satellite image. By 0600 UTC, these cells were organizing into a line of convection over central Ireland (Fig. 4b),

which by 0900 UTC became well defined with a maximum rain rate  $> 16 \text{ mm h}^{-1}$ . Rainfall accumulations of up to 15 mm were measured in Ireland during the passage of the rainband, which lengthened and narrowed slightly in the next 3 h, then moved eastward across the Irish Sea to Scotland and northern England. As this rainband moved away from Ireland, a second rainband developed to the east over Scotland and the North Sea (Fig. 4d) beneath the eastern band of high cloud. Both rainbands eventually dissipated over the northern North Sea late on 16 September.

Radiosonde profiles over Valentia at 0000 UTC and Castor Bay at 1200 UTC, the nearest regular ascents to the rainband under consideration here (Fig. 5), showed low values of CAPE—in the range  $10\text{--}14 \text{ J kg}^{-1}$ , consistent with the September mean of CAPE at Valentia of  $10 \text{ J kg}^{-1}$  (Siedlecki 2009, his Fig. 2). (CAPE values in this paper are calculated using a mean-layer parcel with mean virtual temperature and mixing ratio in the lowest 500 m.) The soundings also showed a deep quasi-moist-adiabatic layer extending from the surface to the upper troposphere, indicative of low convective inhibition (CIN). The general environment was therefore close to neutral stability for deep convection. However, the humidity profiles from the two sondes were markedly different. At 0000 UTC over Valentia, a capping inversion at 700 hPa marked a sudden transition from near saturation to a dry layer (with relative humidity

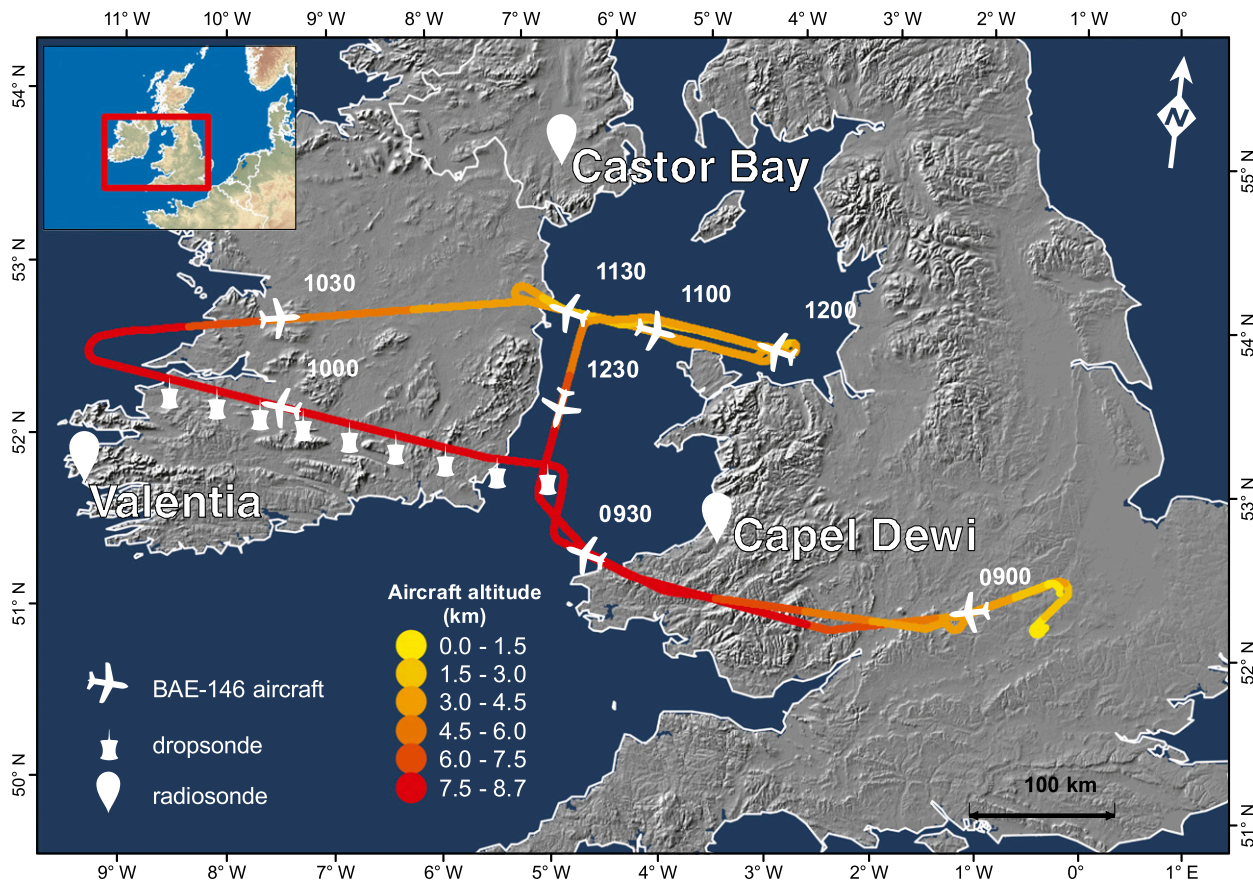


FIG. 9. The track, colored according to altitude (km), of the FAAM BAE-146 aircraft on 16 Sep 2011 during TROSIAD IOP1. The annotations on the track represent the locations where dropsondes were launched. The radiosonde launch sites from Valentia and Castor Bay are also labeled. Radiosondes were launched every 3 h between 0717 and 1901 UTC from Capel Dewi (52.42°N, 4.01°W), near Aberystwyth, Wales, where the U.K. Mesosphere–Stratosphere–Troposphere (MST) radar is located.

about 30%) around 80 hPa deep. Similarly, a radiosonde from Capel Dewi at 1259 UTC, immediately after the passage of the rainband, also showed a capping inversion starting at 700 hPa with dry air above 630 hPa (Fig. 6a), this time with a deep moist absolutely unstable layer (MAUL; Bryan and Fritsch 2000) from the surface to 700 hPa with a CAPE of 708 J kg<sup>-1</sup>. No CIN was present in this sounding either. The existence and large depth of this MAUL was surprising (the second deepest over the 11-yr period 2002–12 from all U.K. radiosonde sites), given the relatively unimpressive nature of the convective rainband when compared to the types of MAULs documented in the United States (Bryan and Fritsch 2000). Thus, the formation of a deep MAUL can occur, even in the absence of a strong convective line.

In contrast, near the northern edge of the rainband, the radiosonde from Castor Bay at 1200 UTC measured a saturated adiabatic profile from 850 hPa to the tropopause at 320 hPa, with no capping inversion. As we shall

see, this is consistent with a marked gradient in the convective cloud top from south to north along the rainband.

The rainband is shown on the surface weather charts (Figs. 3b,d,f) as an occluded front, positioned ahead of the trough axis at 0000 and 0600 UTC, but with its southernmost extension appearing to cross the trough axis at 1200 UTC. A more detailed picture of this part of the band is afforded by the MST radar observations at Capel Dewi. In Fig. 7a, layers of high power ascend over time in the stratosphere (>9 km) and descend in the troposphere. Sloping layers in MST radar power around the tropopause tend to follow isentropic surfaces [e.g., Parton et al. (2009), their Fig. 18], so Fig. 7a shows the passage of the cyclonic PV anomaly around 1200 UTC with isentropic surfaces in the troposphere descending thereafter. A similar pattern of descending layers is shown in the wind shear (Fig. 7b). Here, the convective rainband appeared as the column of variable wind shear below 3 km around 1245 UTC, where the turbulent convection caused large variability in the measured wind

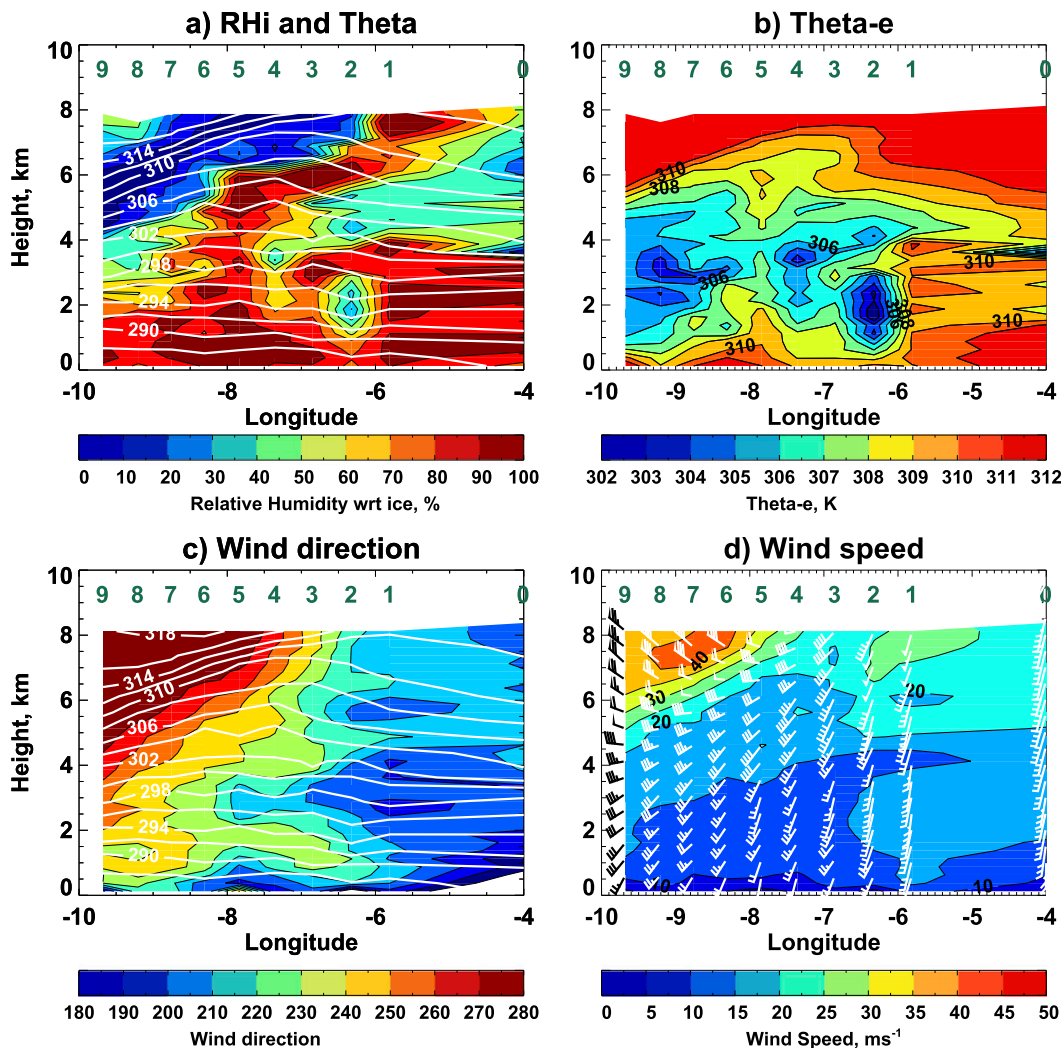


FIG. 10. Cross sections along the track of the FAAM BAe-146 aircraft of (a) relative humidity (% , shaded according to scale) and potential temperature (every 2 K, thin solid lines), (b) equivalent potential temperature ( $\theta_e$ , shaded according to the scale), (c) wind direction ( $^{\circ}$ ) and potential temperature (every 2 K, thin solid lines), and (d) wind speed,  $\text{m s}^{-1}$ , constructed from the nine dropsondes and Capel Dewi radiosonde along  $52.5^{\circ}\text{N}$  (Fig. 9) and horizontal wind (pennant, barb, and half-barb denote wind speeds of 25, 5, and  $2.5 \text{ m s}^{-1}$ , respectively). Relative humidity is calculated with respect to water for temperatures greater than  $0^{\circ}\text{C}$ , and with respect to ice for temperatures lower than  $0^{\circ}\text{C}$ . Sondes were dropped at roughly 4-min intervals (about 33 km apart) between 0938 and 1010 UTC, and the radiosonde was launched at 1014 UTC.

values. Above the turbulence, around 3.6 km, was a layer of weakly enhanced wind shear and strong echo power, which represented the humidity gradient at 630 hPa in the radiosonde profile of Fig. 6a that, combined with the increase in static stability, was capping the convection. A second layer of much more prominent wind shear and weaker enhancement of echo power extended from 8 km at 1200 UTC to 4 km by 1600 UTC. This feature represented the tropopause fold extending downward on the western side of the PV anomaly. Thus, the upper-level PV anomaly at this time had overtaken the convective

rainband—in other words, the rainband at Capel Dewi had moved from beneath the eastern side of the PV anomaly to beneath the western side of the PV anomaly in about 3–4 h. This capping layer is a key player throughout this article.

Surface measurements at Capel Dewi (Fig. 8) show a steady increase in both temperature and dewpoint as the rainband approached, with a maximum dewpoint of  $13.6^{\circ}\text{C}$  at 1320 UTC after the rainband passed over, followed by a drop to  $12^{\circ}\text{C}$  at 1400 UTC and a more gradual decrease thereafter. Surface winds at a nearby



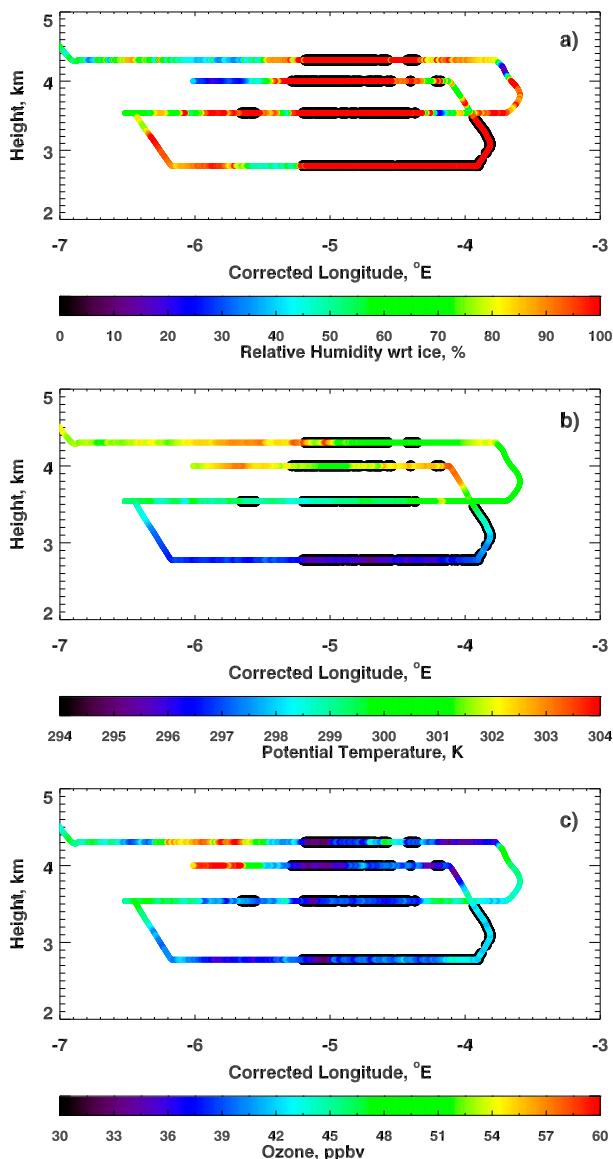


FIG. 11. Cross sections along 53.5°N of (a) relative humidity, (b) potential temperature, and (c) ozone measured by in situ sensors on the aircraft. In-cloud measurements are indicated by the black bands denoting values of liquid water content greater than  $0.1 \text{ g m}^{-3}$ . The longitude values have been adjusted to a common time (referred to as *corrected longitude*) to allow for the  $0.53^\circ \text{ h}^{-1}$  translation speed of the rainband.

hilltop site veered steadily from  $110^\circ$  between 0600 and 0900 UTC to  $255^\circ$  at 1320 UTC, before backing a little to  $240^\circ$  after 1500 UTC (Fig. 8b). A peak in wind speed of  $6 \text{ m s}^{-1}$  was observed from 1100 to 1300 UTC, before a sharp drop to  $4 \text{ m s}^{-1}$  at 1320 UTC. Pressure fell steadily throughout the day until 1600 UTC.

These observations show that the convective rainband developed ahead of the upper-level trough, but by the

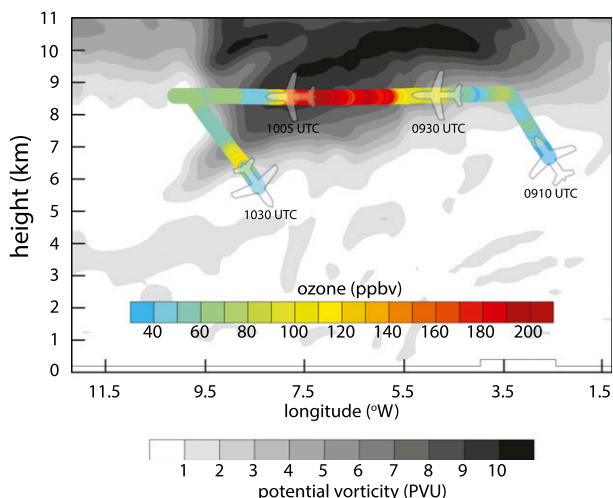


FIG. 12. Potential vorticity from the WRF simulation [PVU ( $1 \text{ PVU} = 10^{-6} \text{ K kg}^{-1} \text{ m}^2 \text{ s}^{-1}$ ), shaded according to the grayscale] and ozone concentration as measured along  $52.5^\circ \text{N}$  between 0910 and 1030 UTC (ppbv, shaded according to the color scale).

time the rainband reached Capel Dewi it lay behind the trough axis. The rainband passed over Capel Dewi between 1230 and 1250 UTC, toward the end of a period of steadily veering surface wind direction and increasing dewpoint, and was capped by a dry, stable layer between 3 and 4 km. Of note is the change in air mass at 1320 UTC, when the temperature decreased by  $1.6^\circ \text{C}$ , wind speed decreased from  $4$  to  $3 \text{ m s}^{-1}$ , and the dewpoint fell by  $1^\circ \text{C}$ . These surface measurements were consistent with the aircraft observations throughout the lower troposphere, presented in the next section.

#### 4. Aircraft observations

The FAAM aircraft took off at 0843 UTC from Cranfield, north of London, and headed westward to Ireland (Fig. 9). The plan was to launch a series of Vaisala RD94 dropsondes across the convective rainband along  $52.5^\circ \text{N}$ , beginning at the edge of Irish airspace at  $5.5^\circ \text{W}$  (permission to drop sondes on the British side of the Irish Sea was denied). Nine dropsondes were released, one every 4 min (about 33 km apart) between 0938 and 1010 UTC.

The first sonde was launched at  $52.54^\circ \text{N}$ ,  $5.81^\circ \text{W}$ , around 20 km west of the center of the convective rainband, and drifted eastward 8 km before landing in the sea. The temperature profile from this sonde generally followed the saturated adiabatic curve from the ground to 8 km, with relative humidity exceeding 80% below 4 km (not shown). A sharp decrease in relative humidity with height at 620 hPa matched that observed at 1259 UTC at Capel Dewi (Fig. 6), but without the

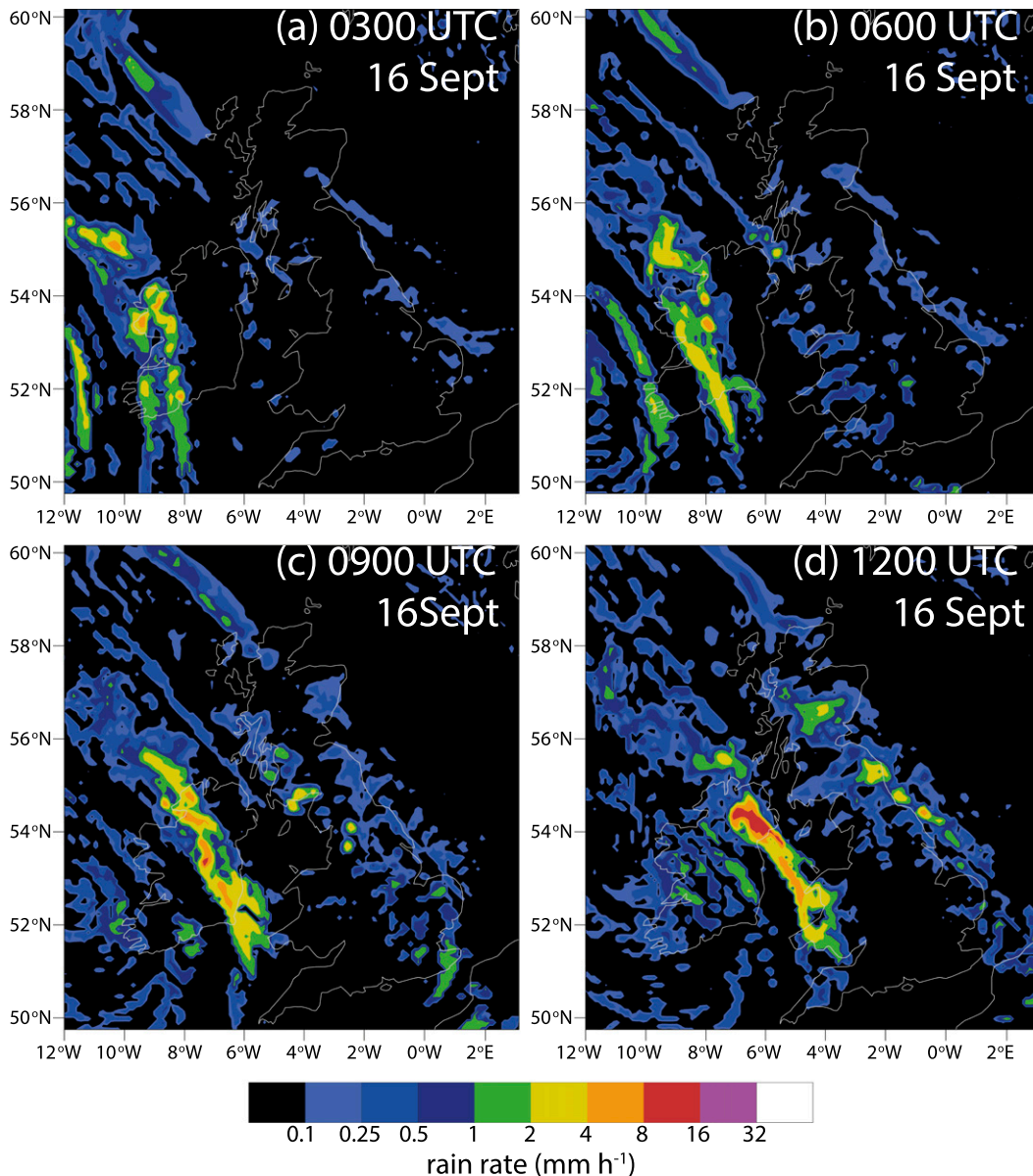


FIG. 13. Rain rate ( $\text{mm h}^{-1}$ , shaded according to the scale) from the WRF simulation at (a) 0300, (b) 0600, (c) 0900, and (d) 1200 UTC 16 Sep.

inversion layer. Furthermore, the near-adiabatic nature of the dropsonde profile showed that the MAUL measured at Capel Dewi was likely to have been a local feature confined to just tens of kilometers in front of the convective rainband itself, consistent with the [Bryan and Fritsch \(2000\)](#) climatology.

A cross section of potential temperature and relative humidity (with respect to ice for temperatures below  $0^{\circ}\text{C}$ ) constructed from the dropsondes is shown in [Fig. 10a](#). This figure is extended to include the radiosonde profile from Capel Dewi at 1014 UTC, but does

not show the convective rainband just east of sonde 1. The cold upper-tropospheric anomaly associated with the depressed tropopause was shown as the bowing up of the isentropes in the upper part of [Fig. 10a](#). On either side of it, the isentropes sloped downward, with the enhanced stability and low relative humidity of the tropopause fold evident on the western side (this was the fold later observed by the MST radar, [Fig. 7b](#)). The low-level profiles of relative humidity and  $\theta_e$  measured by sonde 1 were similar to those measured by the radiosonde 135 km to the east, showing that the rainband

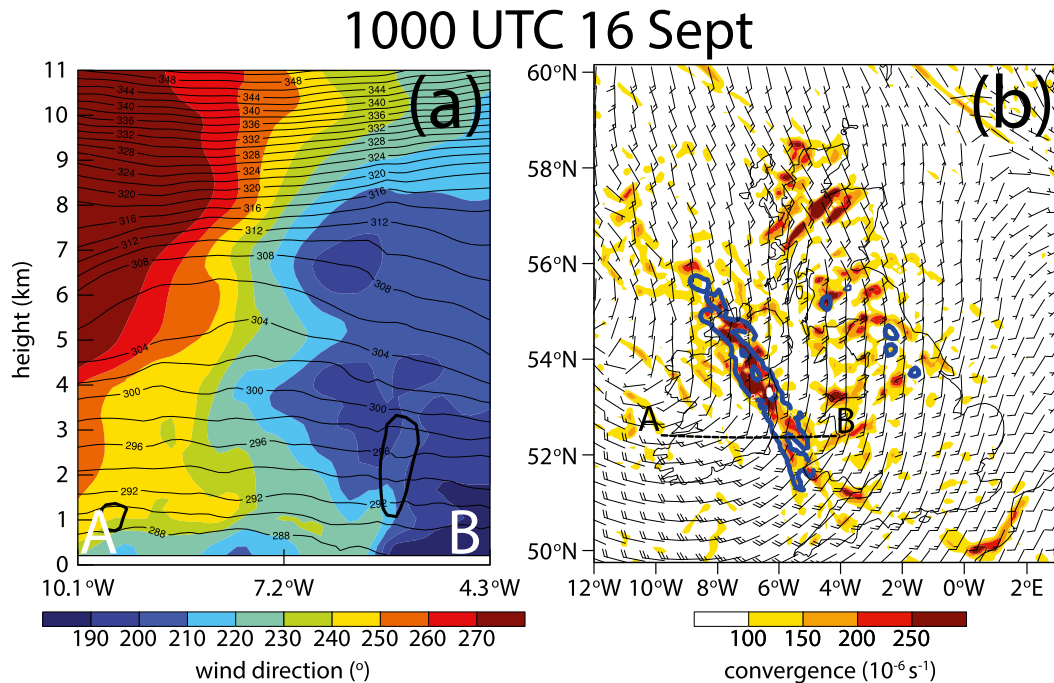


FIG. 14. (a) Cross section along 52°N from the WRF simulation at 1000 UTC 16 Sep showing potential temperature (K, solid lines), wind direction (degrees, colored), and location of precipitation (bold black line). (b) Maximum convergence value below 2 km at 1000 UTC 16 Sep (shaded according to scale in units of  $10^{-6} s^{-1}$ ) and location of precipitation (blue line).

lay in an airstream bringing moister air throughout the lowest 3 km. The sharp gradient in relative humidity to the west of sonde 1 was consistent with that observed at Capel Dewi after the passage of the rainband, suggesting an airmass boundary. The cross section also shows a second region of moist low-level air between 8.5° and 7.5°W, where light precipitation was occurring (Fig. 4).

The dropsonde wind measurements are shown in Figs. 10c and 10d. These show the upper-level wind maximum between 8° and 9°W and a transition from generally westerly low-level winds in the western part of the figure to southerly winds to the east. Most striking on Fig. 10c is a layer of more-westerly winds extending from 6° to 8°W below 2 km, with a rotation of the wind at its tip coinciding with a strengthening of the wind speed to the east. This tip (near sonde 1) is the location of the convective rainband. The rapid change of wind direction at the tip of the westerly layer likely resulted in a line of convergence sufficient to provide the lift needed to initiate convection (in an environment with little to no convective inhibition, moderate instability, and sufficient moisture) and organize it into a rainband. We show in the next section that the convergence line preceded the rainband, rather than developing as part of it.

After dropping the sondes, the aircraft descended through the tropopause fold to perform a series of

in situ legs through the convective rainband between 1030 and 1230 UTC along 53.5°N (Fig. 9), the only location where air-traffic permission for such legs could be obtained on this day. A cross section of relative humidity, equivalent potential temperature, and ozone mixing ratio is shown in Fig. 11. At the lowest level (2.77 km), the cross section was consistent with Fig. 10, with a pronounced dry layer just west of the cloud band. At 3.5 km, there was little change along the flight leg, consistent with the moister region at this altitude in Fig. 10a. By contrast, the two upper legs (at 4.0 and 4.3 km), exhibited a clear change in air mass from west to east, with ozone-rich, dry, and potentially warmer air 1.0°–0.4° west of the cloud band.

No evidence of a capping layer was evident at this location. Indeed, visual observations on board the aircraft reported cloud tops well above 4 km. The measurements of dry, potentially warmer air to the west of the rainband at around 4 km suggests that, at 53.5°N, the air mass that formed the capping layer at Capel Dewi had not caught up with the convective rainband. This is consistent with the cyclonic rotation of the upper-level trough and PV anomaly causing the dry midlevel air to overrun the convection at the southern end but to remain behind it at the northern end. As we discuss in more detail in the next section, this led to the



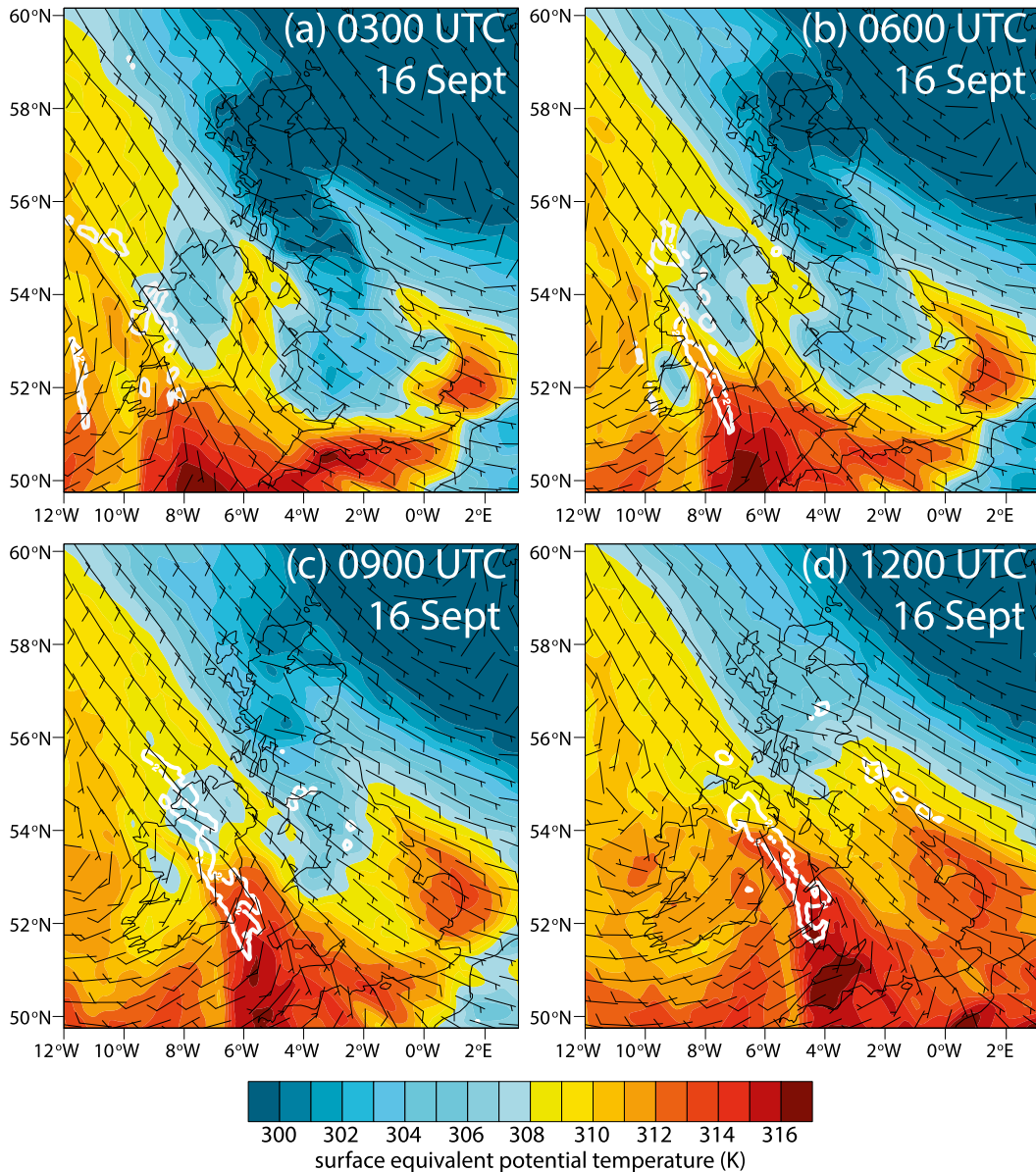


FIG. 15. Surface equivalent potential temperature (K, shaded according to the scale) and 10-m wind (pennant, barb, and half-barb denote wind speeds of 25, 5, and 2.5 m s<sup>-1</sup>, respectively) from the WRF simulation at (a) 0300, (b) 0600, (c) 0900, and (d) 1200 UTC 16 Sep. The white contour surrounds the region where the simulated rain rate was greater than 2 mm h<sup>-1</sup>.

pronounced gradient in cloud top from south to north along the rainband mentioned in section 3a.

## 5. Model simulation of the convective rainband

### a. Comparison with observations

The WRF simulation depicted a cyclonic PV anomaly with similar characteristics to that observed, but progressing a little more slowly eastward. This

difference in timing between the model and the observations is illustrated by Fig. 12 where ozone measurements taken along 52.5°N by the aircraft (between 0910 and 1030 UTC) are plotted over the PV cross section from the model at 1030 UTC [ozone and PV are strongly correlated in the tropopause region, e.g., Danielsen (1968)]. Ozone concentrations exceeding 140 ppbv were present between 5.5° and 7.6°W, as the aircraft flew above the depressed tropopause in the upper-level trough, and exceeded 110 ppbv as the

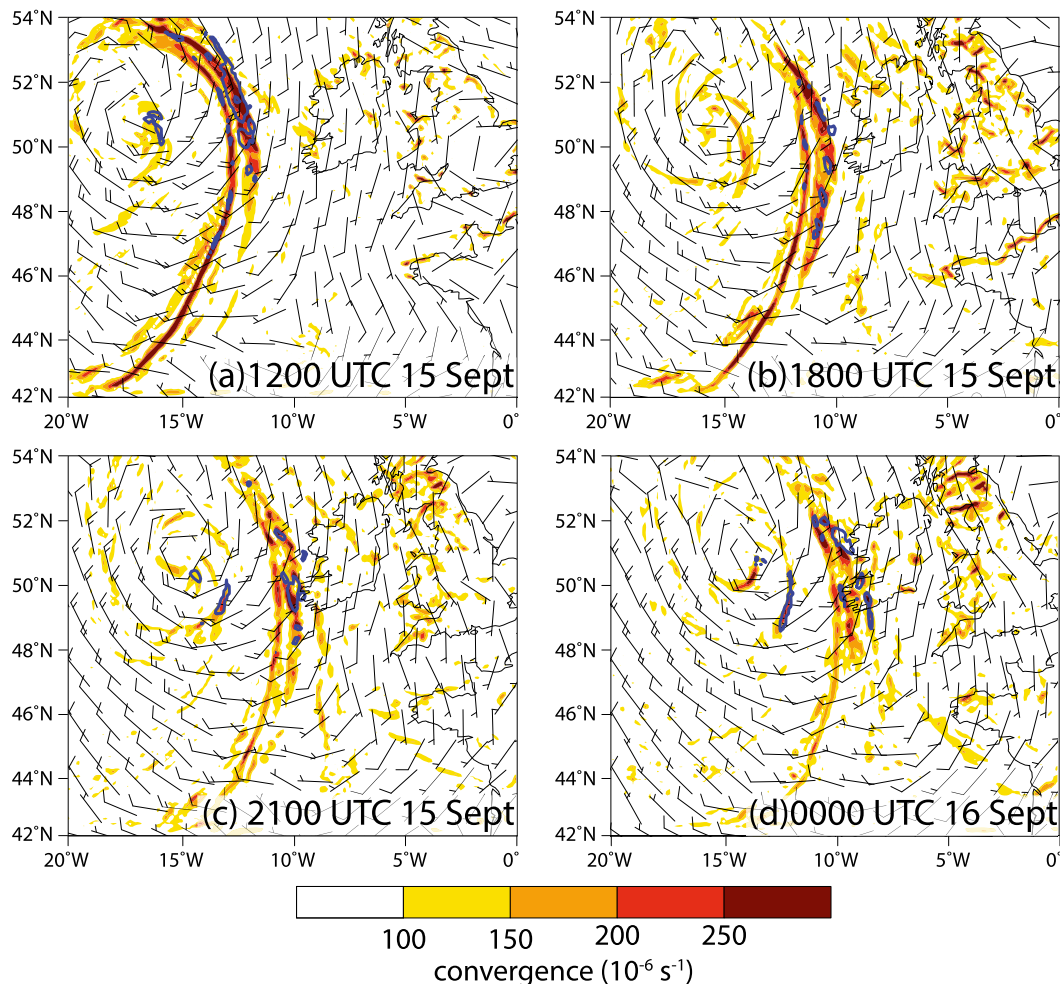


FIG. 16. Maximum convergence below 2 km (shaded according to the scale in units of  $10^{-6} \text{ s}^{-1}$ ), winds at 850 hPa, and regions of precipitation (blue lines) at (a) 1200 UTC 15 Sep, (b) 1800 UTC 15 Sep, (c) 2100 UTC 15 Sep, and (d) 0000 UTC 16 Sep 2011.

aircraft descended through the tropopause fold. The structure was similar in the model PV, but displaced around  $1^\circ$  farther westward, indicative of the slower eastward progression of the cyclone in the model simulation.

As in the radar imagery, the convection appeared in the WRF simulation at 0300 UTC as a broad area of convection, which organized into a single rainband and strengthened in time (Fig. 13). (Note that the convection at 0300 UTC was more organized in the model than in reality.) At 0900 UTC, the observed rainfall rate was heavier than in the model, but the model did not capture the slight weakening of the rainband in the subsequent 3 h, showing a higher rainfall rate at 1200 UTC than at 0900 UTC. These caveats aside, the general position, orientation, and intensification of the rainband was captured by the model simulation.

Figure 14a shows the model cross section of wind direction along  $52^\circ\text{N}$  at 1000 UTC, corresponding to the dropsonde cross section in Fig. 10c. A similar layer of more-westerly wind direction below 2 km was present in the model, with its tip at the location of the convective plume. Confirming that the tip was a region of convergence as well as confluence, Fig. 14b shows the low-level convergence field from the WRF simulation at the same time; the correspondence of convergence and convection is evident, substantiating our hypothesis that the wind rotation measured by the dropsondes coincided with a region of convergence and lift.

The WRF simulation also shows a plume of high- $\theta_e$  ( $>310 \text{ K}$ ) air at the surface, associated with poleward-advancing warm moist air ahead of the surface cyclone and extending northwestward over southwest Ireland

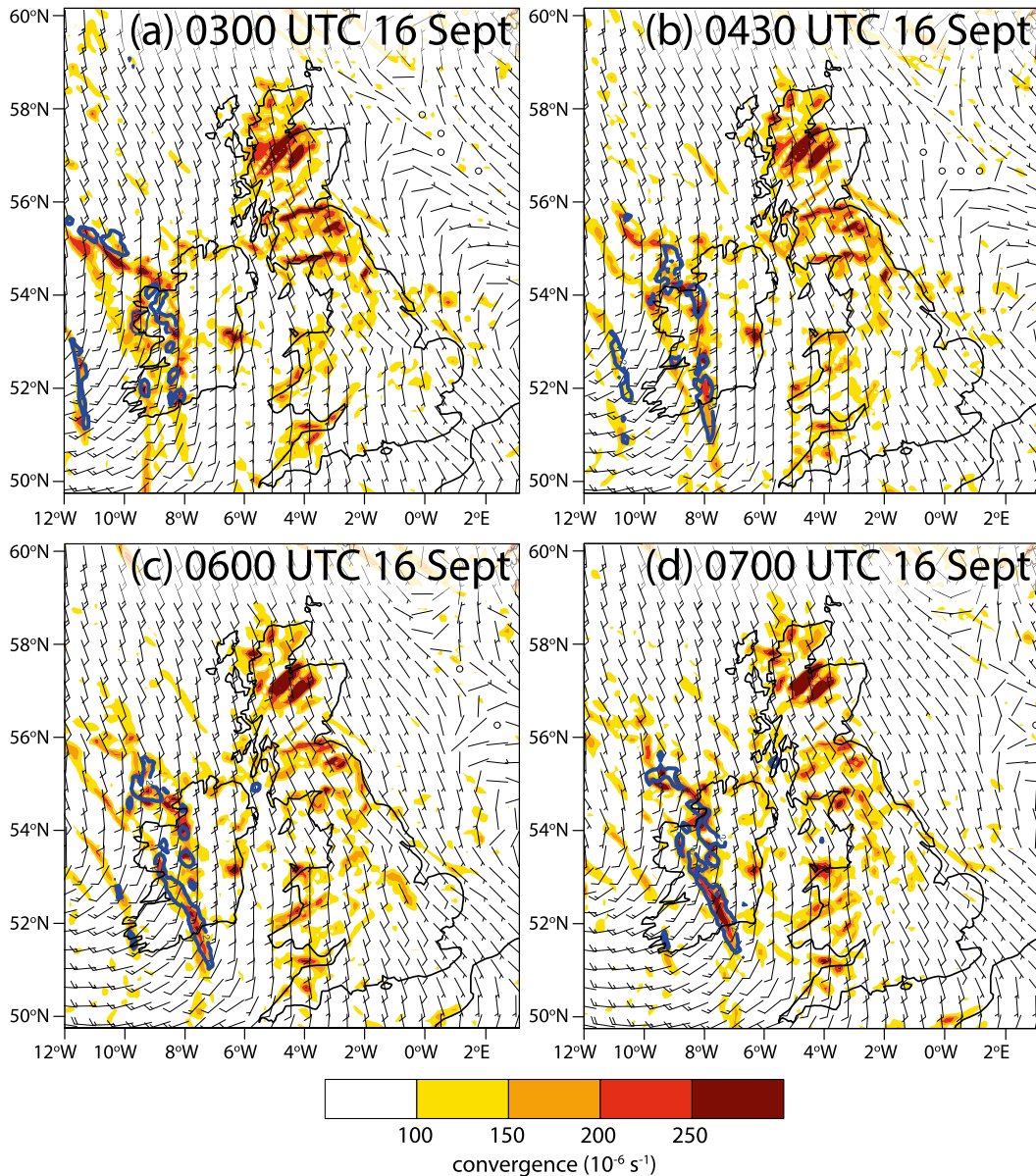


FIG. 17. Maximum convergence below 2 km (shaded according to the scale in units of  $10^{-6} \text{ s}^{-1}$ ), winds at 850 hPa, and regions of precipitation (blue lines) at (a) 0300, (b) 0430, (c) 0600, and (d) 0700 UTC 16 Sep 2011.

at 0300 UTC (Fig. 15a). By 0600 UTC, the plume had been drawn farther northwestward over Ireland, coincident with the most intense part of the rainband (Figs. 15b–d). The eastward and northward march of this plume was consistent with the progression of the southern half of the convection, and the narrow zone of lower  $\theta_e$  immediately behind it, was consistent with the aircraft measurements and the decrease in dewpoint at Capel Dewi after the passage of the rainband (Fig. 8). The model also reproduced the MAUL measured by the radiosonde from Capel Dewi at 1259 UTC (Fig. 6b), though with much smaller vertical

extent and with convection extending higher than in the observed case.

#### b. Evolution of the rainband

We now examine the development of the convective rainband and its relationship to preexisting structures in the wind field, beginning at 1200 UTC 15 September. At this time, the WRF simulation shows two lines of convergence and precipitation (Fig. 16a), near the rear of the frontal cloud band at 14°W (Fig. 1b), corresponding to the front in Fig. 1a. As in the satellite images (Fig. 2), these lines tracked eastward toward



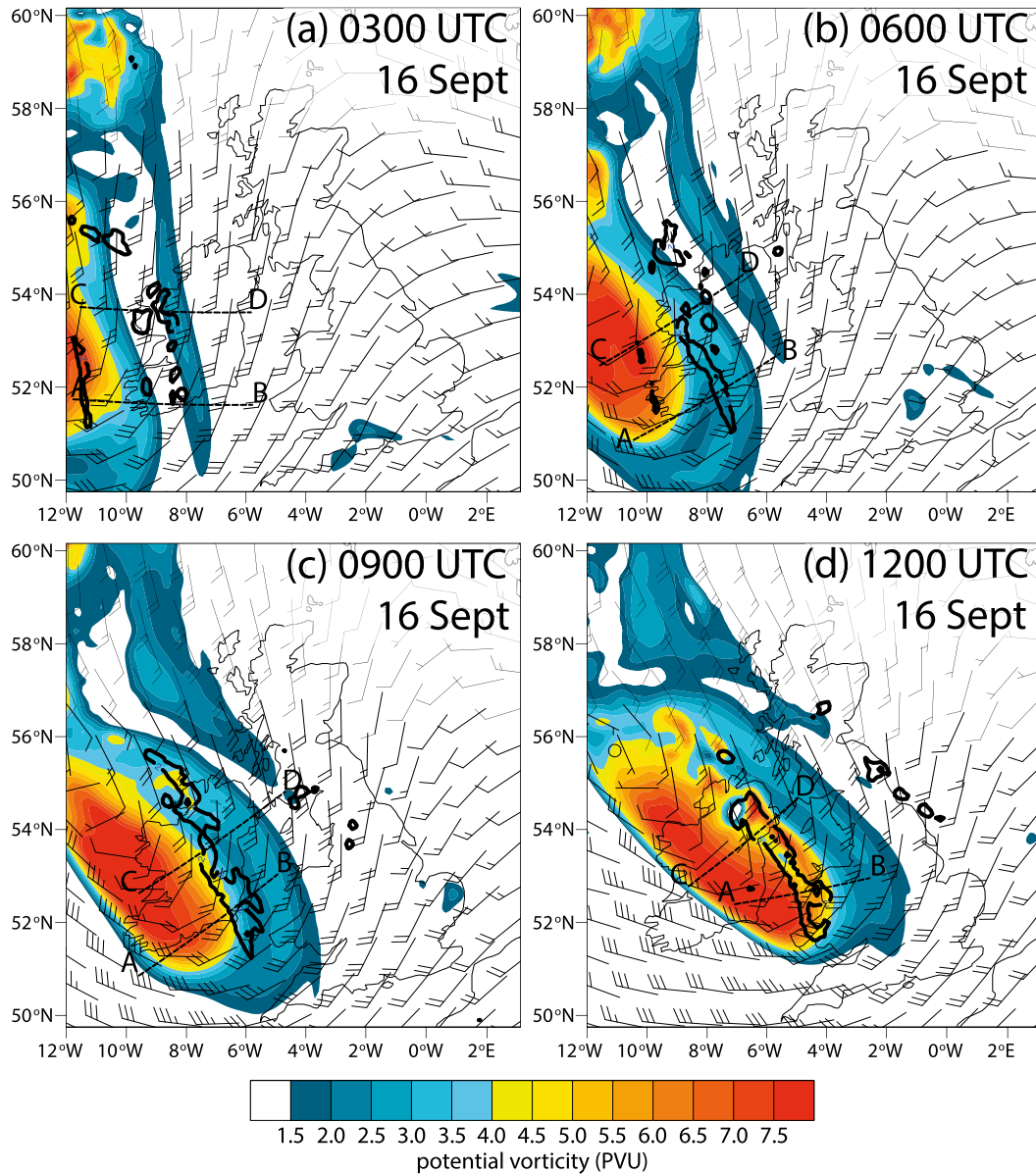


FIG. 18. Potential vorticity (PVU, shaded according to the scale) and wind (pennant, barb, and half-barb denote wind speeds of 25, 5, and 2.5 m s<sup>-1</sup>, respectively) on the 316-K isentropic surface from the WRF simulation, and locations of cross sections AB (Fig. 19) and CD (Fig. 20) at (a) 0300, (b) 0600, (c) 0900, and (d) 1200 UTC 16 Sep. Black contours surround regions where the simulated rain rate was greater than 2 mm h<sup>-1</sup>.

Ireland, maintaining the double convergence line, but with gradually weakening precipitation. At 0300 UTC, three lines of convergence intersected 52°N, around 8°, 9°, and 11°W (Fig. 17a). A line of precipitation coincided with the westernmost convergence line, but there was only patchy precipitation over southwest Ireland where the other two lines were located. Over the next 4 h, as convection along the westernmost line weakened, the two leading convergence lines merged, with precipitation organizing into a single rainband and

intensifying along the merged line. This evolution was consistent with the observations of the intensification of the main rainband during 0300–0600 UTC (Figs. 4b and 4c). (Note also the enhanced low-level humidity around 8°W in Fig. 10a coinciding with patchy precipitation as the remains of the westernmost convective line reached Ireland.) Thus, the convergence lines preceded the development of convection into an organized rainband, which occurred when the two lines merged.

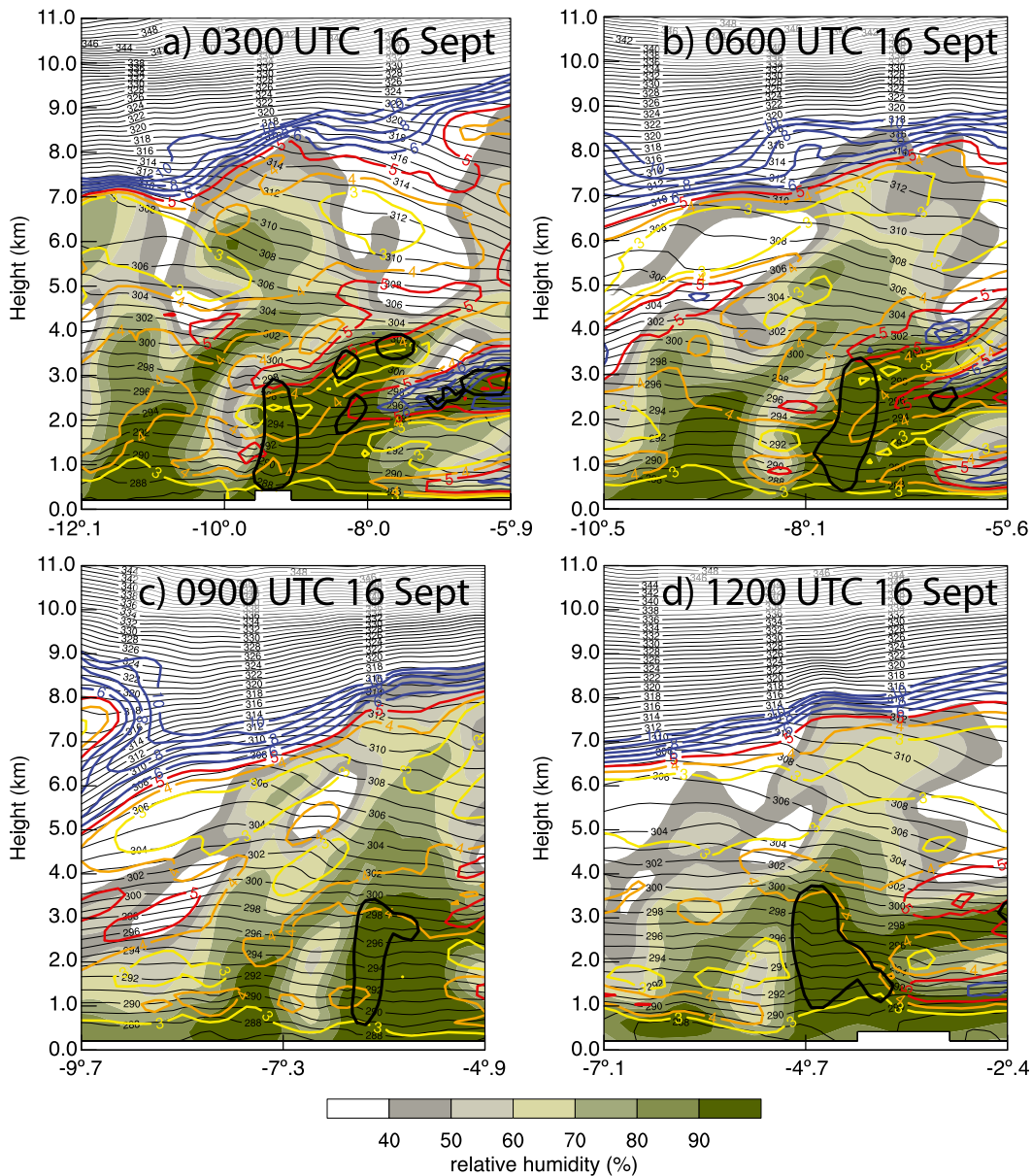


FIG. 19. Vertical cross sections through the southern part of the rainband on 16 Sep 2011 (AB cross sections shown in Fig. 18). Relative humidity (%), shaded according to the scale, potential temperature (black contours every 1 K), static stability (colored contours every 1 K km<sup>-1</sup> between 3 and 10 K km<sup>-1</sup>) at (a) 0300, (b) 0600, (c) 0900, and (d) 1200 UTC 16 Sep. The thick black contours represent the 0.1 g kg<sup>-1</sup> cloud hydrometeor mixing ratio, defined as the sum of the cloud water, snow, and ice mixing ratios. All fields are derived from the WRF simulation.

This merger took place as the frontal remnant reached the Irish coast. To examine whether the movement from ocean to land caused the merger, WRF was simulated again in the same configuration but with Ireland replaced by ocean. The results differed little from those already presented (not shown). They confirm that the merger occurred because of the dynamics of the convergence lines themselves rather than differences in

surface friction or coastal convergence. The alignment of precipitation with the convergence lines, and the intensification of convection after the two leading lines merged, shows that the organization of convection in this case resulted from the remnants of the original front, in the form of low-level wind and humidity features rather than a strong thermal gradient (Fig. 12). Nevertheless, two aspects of the evolution of the

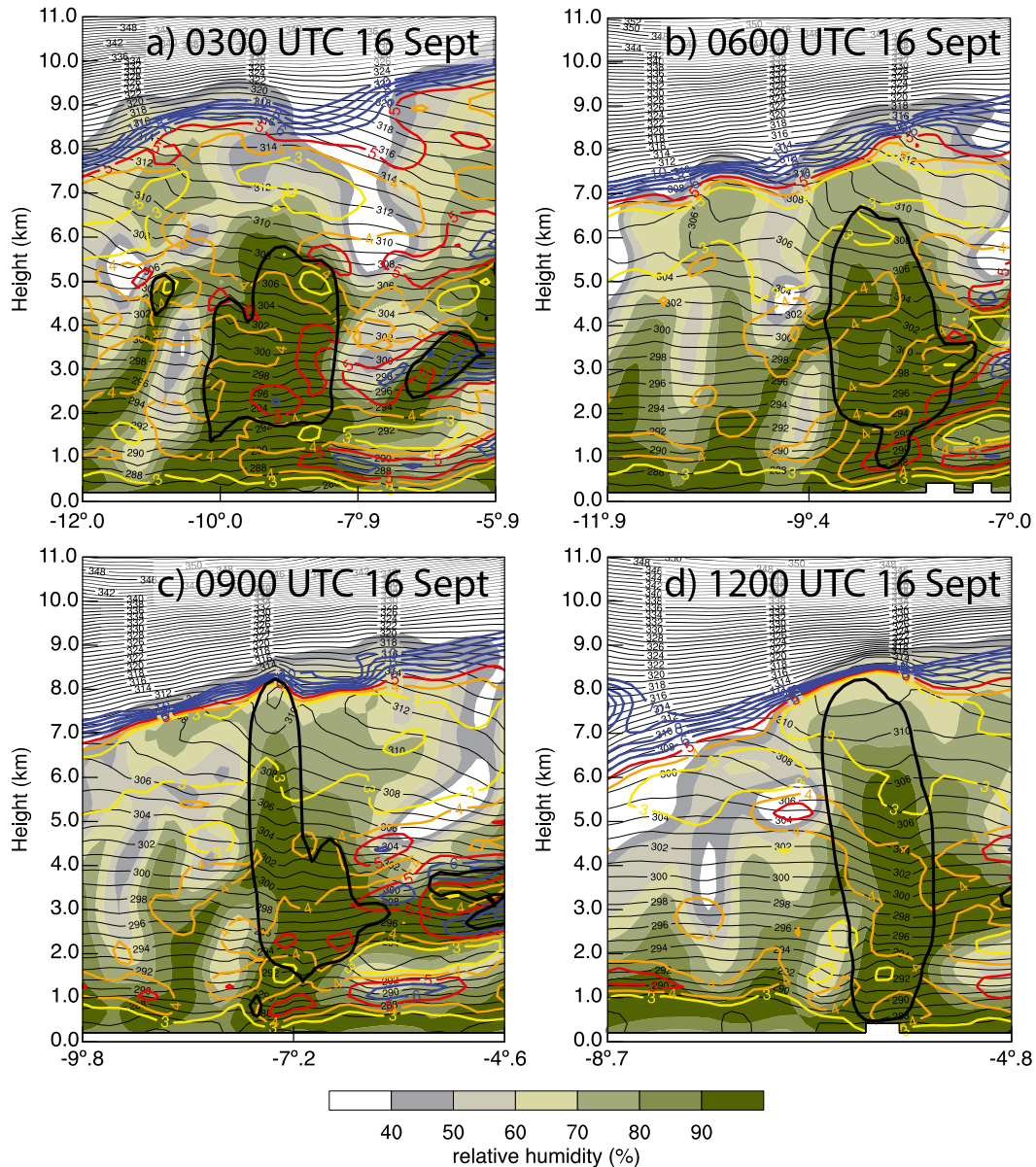


FIG. 20. As in Fig. 19, but for the northern part of the rainband on 16 Sep 2011 (CD cross sections shown in Fig. 18).

rainband are not explained solely by low-level convergence, and it is to these we now turn.

First, Fig. 18 shows the potential vorticity field at 316 K, near the tropopause above the rainband, together with the model precipitation. During 0300–0900 UTC, the rainband clearly lay on the eastern side of the PV maximum (Figs. 18a–c). By 1200 UTC, however, the eastward advance and cyclonic rotation of the PV anomaly was overtaking the southern portion of the rainband (Fig. 18d), a process that happened quicker in reality than in the model and that led to the tropopause fold on the western side of the anomaly appearing above

the convection in Fig. 7. Second, there was a marked gradient in cloud-top height along the rainband both in the model simulation and in the satellite images, from around 4 km in the south to above 8 km in the north. This gradient appears also in the difference between the dropsonde and in situ cross sections measured by the aircraft. To examine this further, we present a series of model cross sections representative of the southern and northern parts of the rainband, along the lines AB and CD in Fig. 18 (Figs. 19 and 20, respectively).

Along the southern cross sections AB, Fig. 19 illustrates the capping of the convection in the southern part



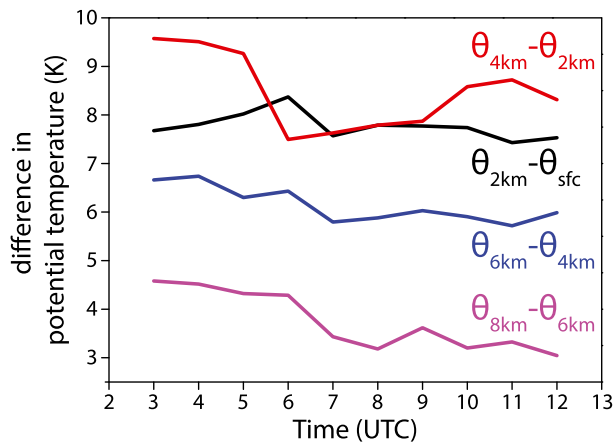


FIG. 21. Evolution of the stability (as  $\Delta\theta$ ), averaged over the northern part of the rainband across four layers: surface–2 km (K, black line), 2–4 km (K, red line), 4–6 km (K, blue line), and 6–8 km (K, magenta line) on 16 Sep 2011. All values are derived from the WRF simulation.

of the rainband by a stable layer between 3 and 4 km, and the location of the convection just east of a gradient in humidity, as in the observations. The tropopause lay between 8.0 km ( $\theta = 316$  K) and 7.5 km ( $\theta = 314$  K), a little lower than the 9 km ( $\theta = 318$  K) in the observed profile (Fig. 6a). By contrast, the northern cross sections CD (Fig. 20) depict convection growing in depth over time and reaching the tropopause (8 km, 311 K) by 0900 UTC. The base of the convection occurred at about 2 km, above a stable boundary layer, and only extended to the surface after 0900 UTC when the boundary layer stability decreased. The deeper convection was consistent with model rain rate increasing during 0900–1200 UTC, in contrast to the observations in which the rain rate decreased (cf. Figs. 13 and 4), suggesting that the details of the boundary layer structure were perhaps not as well captured as the mesoscale and large-scale forcing.

What was the role of the large-scale forcing in this case? A clue may be found in Fig. 21, showing the evolution of static stability over the northern part of the rainband in the model simulation (defined as the average stability within the  $2 \text{ mm h}^{-1}$  rainfall contour in the northern part of the rainband). The decrease in low-level stability ( $\theta_{2\text{km}} - \theta_{\text{sfc}}$ ) after 0600 UTC has already been noted, while that of the lower free troposphere ( $\theta_{4\text{km}} - \theta_{2\text{km}}$ ) increased as the rainband intensified. Above 4 km, however, the stability decreased over time, allowing the convection to reach higher. These stability changes coincided with the approach of the PV anomaly, with isentropes sloping upward in the stratosphere and down in the troposphere as discussed in section 3. The change in stability resulted from the changing position

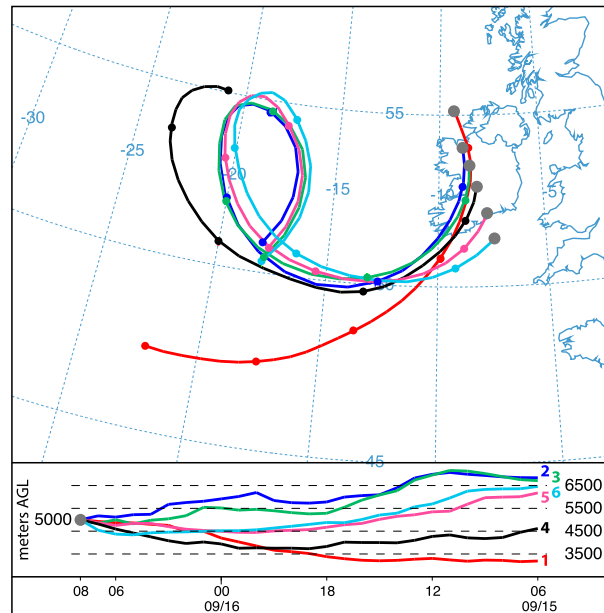


FIG. 22. Isentropic back-trajectories starting from 5 km at 0800 UTC 16 Sep 2011 at locations just behind the convective rainband, calculated with HYSPLIT based on the WRF simulation. The time axis on the bottom plot is reversed.

of the rainband relative to the upper-level PV anomaly (from the east side to the west side). Thus, the change in the environmental static stability associated with the

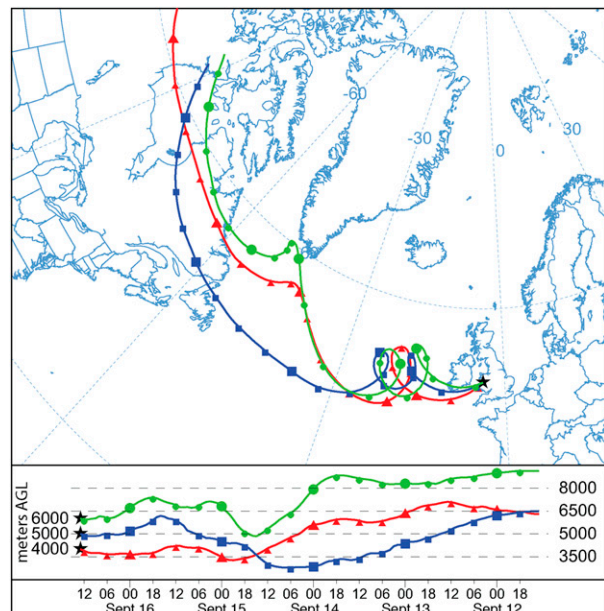


FIG. 23. Representative back-trajectory calculations starting from 4, 5, and 6 km at 1300 UTC 16 Sep above Capel Dewi, calculated with HYSPLIT based on Global Data Assimilation System (GDAS) analyses. The time axis on the bottom plot is reversed.

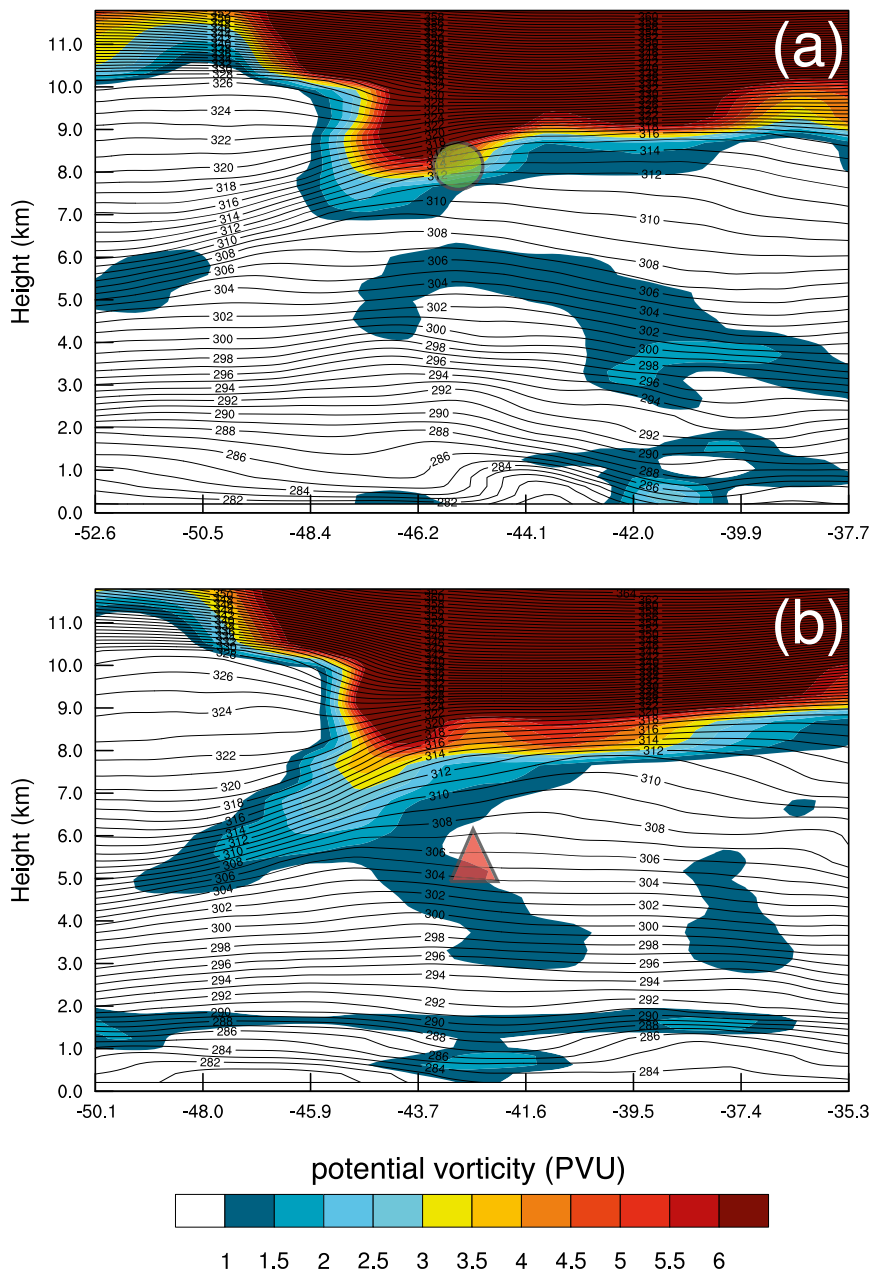


FIG. 24. (a) West-east cross section along 59°N at 0000 UTC 14 Sep using GDAS analyses, showing potential temperature (K, black lines) and potential vorticity (PVU, colored). The green circle denotes the position of the (green) back trajectory initiated at 6 km in Fig. 23 at this time. (b) As in (a), but at 56.2°N, and the location of the (red) trajectory in Fig. 23, initiated at 4 km.

advancing PV anomaly was consistent with the increasing depth (and possibly also intensity) of convection over time in the northern part of the rainband, where the convection was not capped by midtropospheric layers.

What was the role of isentropic upgliding (Hoskins et al. 2003) ahead of the trough? To examine this,

isentropic back-trajectories starting in the midtroposphere between 4 and 6 km were calculated from points around the rainband starting at 0800 UTC 16 September, using HYSPLIT (Stein et al. 2015) based on 30-min output from the WRF simulation. Two-dimensional isentropic trajectories rather than three-dimensional kinematic trajectories were

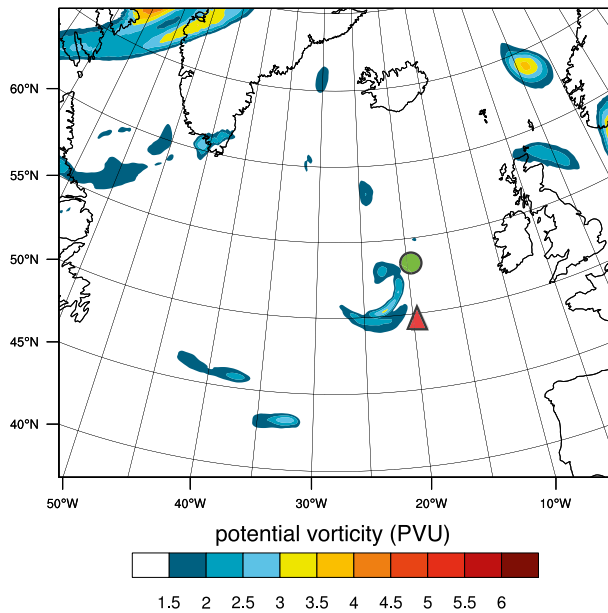


FIG. 25. Potential vorticity field at 315 K at 0000 UTC 15 Sep, showing the dissociation of the streamer from the PV reservoir and the positions of the green and red trajectories in Fig. 23 along its flank at this time.

used to isolate the synoptic-scale component of the vertical velocity. Ahead of the rainband, the trajectories did indeed ascend downstream of the trough axis, by around  $3 \text{ cm s}^{-1}$  (not shown), consistent with the magnitude of synoptic-scale ascent expected in an extratropical cyclone. Just behind the rainband, however, a rather different picture emerges. Trajectories starting in this region at 5 km are shown in Fig. 22. The three southern starting locations (4, 5, and 6 in Fig. 22) ascended downstream of the trough axis, but the next two (trajectories 2 and 3) consistently descended. Only the most northerly starting location corresponded to consistent ascent from well south of the trough, in a manner similar to a warm conveyor belt. Trajectories started at other heights between 4 and 6 km differed in detail but also showed a mixture of recent ascent and recent descent. Taken together, these trajectories show that the airstream downstream of this upper-level trough did not always correspond to the paradigm of isentropic upgliding, and, even when it did, most of the trajectories (including those from starting locations ahead of the rainband) originated in descending flow upstream of the trough axis and descended at least an equivalent amount to their subsequent ascent. The reduction in convective inhibition and increase in relative humidity of the ascending airstream would therefore only compensate for changes in the opposite sense directly upstream.

We conclude that isentropic upglide probably played little part in conditioning the airstream to convection in this case.

### c. Effect of tropopause folds

Despite the favorable synoptic conditions, convection over the southern part of the rainband was capped by a dry, stable layer around 4-km altitude (600 hPa, or  $\theta = 298 \text{ K}$ , Fig. 6). To examine the origin of this layer, HYSPLIT three-dimensional kinematic back-trajectories calculated from Capel Dewi based on global analysis fields were initialized at 1300 UTC 16 September. Back-trajectories starting in the moister, less stable air at 5 km (533 hPa,  $\theta = 305 \text{ K}$ , Fig. 23) ascended from around 3 km over the mid-Atlantic in the previous 2.5 days. However, trajectories initialized in the stable capping layer at 4 km and the tropopause fold at 6 km (466 hPa,  $\theta = 310 \text{ K}$ ) both descended from a location just south of Greenland around three days previously. Cross sections across the north–south flow at  $59^\circ$  and  $56.2^\circ \text{ N}$  at 0000 UTC 14 September are shown in Fig. 24, together with the back-trajectory locations at this time. These show that the air observed at 6 km over Capel Dewi originated near the base of a tropopause fold, on the flank of a streamer of stratospheric PV that extended southward over the mid-Atlantic and that eventually broke away from the main stratospheric PV reservoir and rolled up into the cyclone shown in Fig. 3 (Fig. 25). The air observed at 4-km tracks back to a region of elevated PV below the fold. Continuing this back further, it originated from an upstream fold on the flank of a PV streamer around  $70^\circ \text{ N}$ ,  $120^\circ \text{ W}$  at 1200 UTC 11 September (not shown).

The 6-km trajectory shown in Fig. 23 is representative of the region within  $0.5^\circ$  of Capel Dewi (trajectories initiated at this height within  $0.5^\circ$  followed essentially the same path). The same is true of the 4-km trajectory, except for initiating points northeast of the site, ahead of the lower dry, stable layer. By contrast, over the northern part of the rainband, back-trajectories proved to be very sensitive to the starting location, with origins in the boundary layer or the tropopause region from starting points  $0.1^\circ$  apart. This sensitivity was consistent with the sharp airmass contrast near the rainband in the aircraft in situ data (Fig. 11), so conclusions on airmass origins cannot be drawn from trajectory calculations at this location. Nevertheless, the Capel Dewi trajectories add to the evidence of Russell et al. (2008, 2009, 2012) that dry, stable layers originating in distant tropopause folds can cap the vertical extent of convection on the eastern side of a trough. As in those cases, a stable layer originating in a tropopause fold well upstream of the current



cyclone had wrapped into it and was capping the convection in the southern part of the rainband.

## 6. Summary

The convection climatology presented by Antonescu et al. (2013) highlighted the prevalence of organized convection in the region east of an upper-level PV anomaly over the United Kingdom, with multicellular linear convection the most common category of organization. To understand the interplay between the synoptic-scale PV anomalies and convection, we used both observations and a mesoscale model simulation to examine a case study of an organized convective rainband that developed and intensified ahead of a cyclonic upper-level PV anomaly. The study answered the primary question addressed in the introduction—the organization of the rainband was the result of low-level convergence associated with a weakening occluded front. This convergence line was associated with an airmass change, with a moister southerly airstream ahead of a drier, more-westerly one, thus providing two of the ingredients (moisture and lift) necessary for deep moist convection (Johns and Doswell 1992). The third ingredient, convective instability, was rather weak in the environment around the convection, but in the absence of convective inhibition (CIN), the northern part of the rainband was able to reach the tropopause, assisted by a reduction in upper-tropospheric static stability as the PV anomaly approached the rainband (cf. Figs. 18c and 18d). The southern part of the rainband only reached a height of about 4 km, limited by a midtropospheric stable layer, the result of a tropopause fold that had wrapped around the PV anomaly. Thus, the main effect of the PV anomaly in this case was to bring reduced stability to the upper troposphere as it approached the rainband, thus allowing the convection to reach higher. The role of isentropic upgliding ahead of the trough appears to have been minor—most of the trajectories examined in this work descended before commencing their upglide, and some did not ascend at all.

The intensification of the rainband occurred as two convergence lines merged between 0400 and 0700 UTC 16 September. These convergence lines originated in an occluded front present to the east of the cyclone the previous day, which had lost its temperature gradient by 0600 UTC 16 September. As well as the merged (and intensified) convergence line, the frontal remnant displayed a humidity gradient, with the wind veer associated with the convergence line drawing a plume of moister air from the south ahead of the southern part of the rainband. Thus, the convection in this case was initiated by the low-level convergence line, not the

upper-level PV anomaly. The effect of the latter was to make the synoptic environment conducive to convection and to modulate its vertical extent.

To the extent that this case can be generalized to other convective rainbands in cyclones, we propose that the prevalence of such rainbands to the east of cyclonic upper-level PV anomalies is related more to the low-level moisture and wind fields than to tropopause-layer forcing, and, in particular, that preexisting moisture gradients and convergence lines (in this case, an old weakening occluded front) are largely responsible for the location and organization of convection. The role of the PV anomaly is more complex than simply providing upgliding. Specifically, the cyclonic low-level flow brings moisture from the south, confluent low-level flow enhances convergence, and tropopause-fold remnants circulating around the midlevel trough cap convection well below the tropopause. Thus, this work further contributes to evidence challenging and clarifying the role of synoptic-scale processes in convection.

*Acknowledgments.* We thank the Natural Environment Research Council (NERC) Mesosphere–Stratosphere–Troposphere radar facility and the Facility for Airborne Atmospheric Measurements for providing measurements for this study, and the NERC Satellite Receiving Station at Dundee University, Scotland, for providing satellite imagery. These datasets were supplied by the British Atmospheric Data Centre (BADC). The work was supported by NERC as part of the Tropopause Folding, Stratospheric Intrusions and Deep Convection (TROSIAD) project, Grant NE/H008225/1 and Diabatic Influence on Mesoscale Structures in Extratropical Storms (DIAMET) project, Grant NE/I005234/1. Antonescu was partially supported by the AXA Research Fund, and Antonescu and Schultz were partially supported by NERC Grant NE/N003918/1. We thank the two anonymous reviewers for their comments.

## REFERENCES

- Antonescu, B., G. Vaughan, and D. M. Schultz, 2013: A five-year radar-based climatology of tropopause folds and deep convection over Wales, United Kingdom. *Mon. Wea. Rev.*, **141**, 1693–1707, doi:10.1175/MWR-D-12-00246.1.
- Browning, K. A., and N. M. Roberts, 1994: Use of satellite imagery to diagnose events leading to frontal thunderstorms: Part I of a case study. *Meteor. Appl.*, **1**, 303–310, doi:10.1002/met.5060010401.
- , —, and C. S. Sim, 1996: A mesoscale vortex diagnosed from combined satellite and model data. *Meteor. Appl.*, **3**, 1–4, doi:10.1002/met.5060030101.
- , and Coauthors, 2007: The Convective Storm Initiation Project. *Bull. Amer. Meteor. Soc.*, **88**, 1939–1955, doi:10.1175/BAMS-88-12-1939.

- Bryan, G. H., and J. M. Fritsch, 2000: Moist absolute instability: The sixth static stability state. *Bull. Amer. Meteor. Soc.*, **81**, 1207–1230, doi:10.1175/1520-0477(2000)081<1287:MAITSS>2.3.CO;2.
- Chen, F., and J. Dudhia, 2001: Coupling an advanced land surface–hydrology model with the Penn State–NCAR MM5 modeling system. Part I: Model implementation and sensitivity. *Mon. Wea. Rev.*, **129**, 569–585, doi:10.1175/1520-0493(2001)129<0569:CAALSH>2.0.CO;2.
- Danielsen, E. F., 1968: Stratospheric-tropospheric exchange based on radioactivity, ozone and potential vorticity. *J. Atmos. Sci.*, **25**, 502–518, doi:10.1175/1520-0469(1968)025<0502:STEBOR>2.0.CO;2.
- Doswell, C. A., III, and L. F. Bosart, 2001: Extratropical synoptic-scale processes and severe convection. *Severe Convective Storms*, C. A. Doswell, III, Ed., Amer. Meteor. Soc., 27–70.
- Dudhia, J., 1989: Numerical study of convection observed during the Winter Monsoon Experiment using a mesoscale two-dimensional model. *J. Atmos. Sci.*, **46**, 3077–3107, doi:10.1175/1520-0469(1989)046<3077:NSOCOD>2.0.CO;2.
- Ek, M. B., K. E. Mitchell, Y. Lin, E. Rogers, P. Grunmann, V. Koren, G. Gayno, and J. D. Tarpley, 2003: Implementation of Noah land surface model advances in the National Centers for Environmental Prediction operational mesoscale Eta model. *J. Geophys. Res.*, **108**, 8851, doi:10.1029/2002JD003296.
- Funatsu, B. M., and D. W. Waugh, 2008: Connections between potential vorticity intrusions and convection in the eastern tropical Pacific. *J. Atmos. Sci.*, **65**, 987–1002, doi:10.1175/2007JAS2248.1.
- Gage, K. S., and J. L. Green, 1978: Evidence for specular reflection from monostatic VHF radar observations of the stratosphere. *Radio Sci.*, **13**, 991–1001, doi:10.1029/RS013i006p00991.
- Gold, D. A., and J. W. Nielsen-Gammon, 2008: Potential vorticity diagnosis of the severe convective regime. Part IV: Comparison with modeling simulations of the Moore tornado outbreak. *Mon. Wea. Rev.*, **136**, 1612–1629, doi:10.1175/2007MWR2093.1.
- Golding, B. W., 1998: Nimrod: A system for generating automated very short range forecasts. *Meteor. Appl.*, **5**, 1–16, doi:10.1017/S1350482798000577.
- Harrison, D. L., R. W. Scovell, and M. Kitchen, 2009: High-resolution precipitation estimates for hydrological uses. *Proc. ICE-Water Manage.*, **162**, 125–135, doi:10.1680/wama.2009.162.2.125.
- Hong, S.-Y., Y. Noh, and J. Dudhia, 2006: A new vertical diffusion package with an explicit treatment of entrainment processes. *Mon. Wea. Rev.*, **134**, 2318–2341, doi:10.1175/MWR3199.1.
- Hoskins, B. J., M. E. McIntyre, and A. W. Robertson, 1985: On the use and significance of isentropic potential vorticity maps. *Quart. J. Roy. Meteor. Soc.*, **111**, 877–946, doi:10.1002/qj.49711147002.
- , M. Pedder, and D. W. Jones, 2003: The omega equation and potential vorticity. *Quart. J. Roy. Meteor. Soc.*, **129**, 3277–3303, doi:10.1256/qj.02.135.
- Johns, R. B., and C. A. Doswell III, 1992: Severe local storms forecasting. *Wea. Forecasting*, **7**, 588–612, doi:10.1175/1520-0434(1992)007<0588:SLSF>2.0.CO;2.
- Juckes, M., and R. K. Smith, 2000: Convective destabilization by upper-level troughs. *Quart. J. Roy. Meteor. Soc.*, **126**, 111–123, doi:10.1002/qj.49712656206.
- Kain, J. S., 2004: The Kain–Fritsch convective parameterization: An update. *J. Appl. Meteor.*, **43**, 170–181, doi:10.1175/1520-0450(2004)043<0170:TKCPAU>2.0.CO;2.
- , and J. M. Fritsch, 1990: A one-dimensional entraining/detraining plume model and its application in convective parameterization. *J. Atmos. Sci.*, **47**, 2784–2802, doi:10.1175/1520-0469(1990)047<2784:AODEPM>2.0.CO;2.
- , and —, 1993: Convective parameterization for mesoscale models: The Kain–Fritsch scheme. *The Representation of Cumulus Convection in Numerical Models*, Meteor. Monogr., No. 24, Amer. Meteor. Soc., 165–170.
- Kitchen, M., and A. J. Illingworth, 2011: The UK weather radar network—Past, present and future. *Weather*, **66**, 291–297, doi:10.1002/wea.861.
- Mlawer, E. J., S. J. Taubman, P. D. Brown, M. J. Iacono, and S. A. Clough, 1997: Radiative transfer for inhomogeneous atmosphere: RRTM, a validated correlated-k model for the longwave. *J. Geophys. Res.*, **102**, 16 663–16 682, doi:10.1029/97JD00237.
- Morrison, H., J. A. Curry, and V. I. Khvorostyanov, 2005: A new double-moment microphysics parameterization for application in cloud and climate models. Part I: Description. *J. Atmos. Sci.*, **62**, 1665–1677, doi:10.1175/JAS3446.1.
- , G. Thompson, and V. Tatarskii, 2009: Impact of cloud microphysics on the development of trailing stratiform precipitation in a simulated squall line: Comparison of one- and two-moment schemes. *Mon. Wea. Rev.*, **137**, 991–1007, doi:10.1175/2008MWR2556.1.
- Newton, C. W., 1954: Frontogenesis and frontolysis as a three-dimensional process. *J. Meteor.*, **11**, 449–461, doi:10.1175/1520-0469(1954)011<0449:FAFAAT>2.0.CO;2.
- , 1958: Variations in frontal structure of upper-level troughs. *Geophysica*, **6**, 357–375.
- Nielsen-Gammon, J. W., and D. A. Gold, 2008: Potential vorticity diagnosis of the severe convective regime. Part II: The impact of idealized PV anomalies. *Mon. Wea. Rev.*, **136**, 1582–1592, doi:10.1175/2007MWR2091.1.
- Parton, G., G. Vaughan, E. G. Norton, K. A. Browning, and P. A. Clark, 2009: Wind profiler observations of a sting jet. *Quart. J. Roy. Meteor. Soc.*, **135**, 663–680, doi:10.1002/qj.398.
- Rao, T. N., J. Arvelius, and S. Kirkwood, 2008: Climatology of tropopause folds over a European Arctic station (Esrange). *J. Geophys. Res.*, **113**, 1–10, doi:10.1029/2007JD009638.
- Reed, R. J., 1955: A study of a characteristic type of upper-level frontogenesis. *J. Meteor.*, **12**, 226–237, doi:10.1175/1520-0469(1955)012<0226:ASOACT>2.0.CO;2.
- , and F. Sanders, 1953: An investigation of the development of a mid-tropospheric frontal zone and its associated vorticity field. *J. Meteor.*, **10**, 338–349, doi:10.1175/1520-0469(1953)010<0338:AIOTDO>2.0.CO;2.
- Reid, H. J., and G. Vaughan, 2004: Convective mixing in a tropopause fold. *Quart. J. Roy. Meteor. Soc.*, **130**, 1195–1212, doi:10.1256/qj.03.21.
- Russell, A., G. Vaughan, E. G. Norton, C. J. Morcrette, K. A. Browning, and A. M. Blyth, 2008: Convective inhibition beneath an upper-level PV anomaly. *Quart. J. Roy. Meteor. Soc.*, **134**, 371–383, doi:10.1002/qj.214.
- , —, —, H. M. A. Ricketts, C. J. Morcrette, T. J. Hewison, K. A. Browning, and A. M. Blyth, 2009: Convection forced by a descending dry layer and low-level moist convergence. *Tellus*, **61A**, 250–263, doi:10.1111/j.1600-0870.2008.00382.x.
- , —, and —, 2012: Large-scale potential vorticity anomalies and deep convection. *Quart. J. Roy. Meteor. Soc.*, **138**, 1627–1639, doi:10.1002/qj.1875.
- Sandhya, M., and S. Sridharan, 2014: Observational relations between potential vorticity intrusions and pre-monsoon rainfall

- over Indian sector. *Atmos. Res.*, **137**, 80–90, doi:[10.1016/j.atmosres.2013.09.013](https://doi.org/10.1016/j.atmosres.2013.09.013).
- Schlemmer, L., O. Martius, M. Sprenger, C. Schwierz, and A. Twitchett, 2010: Disentangling the forcing mechanisms of a heavy precipitation event along the Alpine south side using potential vorticity inversion. *Mon. Wea. Rev.*, **138**, 2336–2353, doi:[10.1175/2009MWR3202.1](https://doi.org/10.1175/2009MWR3202.1).
- Schumann, M. R., and P. J. Roebber, 2010: The influence of upper-tropospheric potential vorticity on convective morphology. *Mon. Wea. Rev.*, **138**, 463–474, doi:[10.1175/2009MWR3091.1](https://doi.org/10.1175/2009MWR3091.1).
- Siedlecki, M., 2009: Selected instability indices in Europe. *Theor. Appl. Climatol.*, **96**, 85–94, doi:[10.1007/s00704-008-0034-4](https://doi.org/10.1007/s00704-008-0034-4).
- Skamarock, W. C., and Coauthors, 2008: A description of the Advanced Research WRF version 3. NCAR Tech. Note NCAR/TN-475+STR, 113 pp., doi:[10.5065/D68S4MVH](https://doi.org/10.5065/D68S4MVH).
- Stein, A. F., R. R. Draxler, G. D. Rolph, M. D. Stunder, M. D. Cohen, and F. Ngan, 2015: NOAA's HYSPLIT atmospheric transport and dispersion modeling system. *Bull. Amer. Meteor. Soc.*, **96**, 2059–2077, doi:[10.1175/BAMS-D-14-00110.1](https://doi.org/10.1175/BAMS-D-14-00110.1).
- Vaughan, G., 2002: The UK MST radar. *Weather*, **57**, 69–73.
- , and Coauthors, 2015: Cloud banding and winds in intense European cyclones: Results from the DIAMET Project. *Bull. Amer. Meteor. Soc.*, **96**, 249–265, doi:[10.1175/BAMS-D-13-00238.1](https://doi.org/10.1175/BAMS-D-13-00238.1).
- Waugh, D. W., 2005: Impact of potential vorticity intrusions on subtropical upper tropospheric humidity. *J. Geophys. Res.*, **110**, D11305, doi:[10.1029/2004JD005664](https://doi.org/10.1029/2004JD005664).
- , and B. M. Funatsu, 2003: Intrusions into the tropical upper troposphere: Three-dimensional structure and accompanying ozone and OLR distributions. *J. Atmos. Sci.*, **60**, 637–653, doi:[10.1175/1520-0469\(2003\)060<0637:IITTUT>2.0.CO;2](https://doi.org/10.1175/1520-0469(2003)060<0637:IITTUT>2.0.CO;2).
- , and L. M. Polvani, 2000: Climatology of intrusions into the tropical upper troposphere. *Geophys. Res. Lett.*, **27**, 3857–3860, doi:[10.1029/2000GL012250](https://doi.org/10.1029/2000GL012250).